

Cluster Catalysis with Lattice Oxygen: Tracing Oxygen Transport from a Magnetite(001) Support onto Small Pt Clusters

Sebastian Kaiser,^{1,2} Farahnaz Maleki,³ Ke Zhang,^{1,2} Wolfgang Harbich,⁴ Ueli Heiz,^{1,2} Sergio Tosoni,³ Barbara A. J. Lechner,^{1,} Gianfranco Pacchioni,³ Friedrich Esch^{1,2}*

¹ Chair of Physical Chemistry, Department of Chemistry, Technical University of Munich,
Lichtenbergstr. 4, 85748 Garching, Germany

² Catalysis Research Center, Technical University of Munich, Lichtenbergstr. 4, 85748 Garching,
Germany

³ Dipartimento di Scienza dei Materiali, University of Milano-Bicocca, via Roberto Cozzi 55,
20125 Milano, Italy

⁴ Institute of Physics, Ecole Polytechnique Fédérale de Lausanne, CH-1015 Lausanne, Switzerland

* bajlechner@tum.de

ABSTRACT. Oxidation catalysis on reducible oxide-supported small metal clusters often involves lattice oxygen. In the present work, we trace the path of lattice oxygen from $\text{Fe}_3\text{O}_4(001)$ onto small Pt clusters during the CO oxidation, aiming at differentiating whether the reaction takes place at the cluster/support interface or on the cluster. While oxygen vacancies form on many other supports, magnetite maintains its surface stoichiometry upon reduction thanks to a high cation mobility. In order to investigate whether size-dependent oxygen affinities play a role, we study two specific cluster sizes, Pt_5 and Pt_{19} . By separating different reaction steps in our experiment, lattice oxygen can be accumulated on the clusters. Temperature programmed desorption (TPD) and sophisticated pulsed valve experiments indicate that the CO oxidation takes place on the Pt clusters rather than at the interface. Scanning tunneling microscopy (STM) shows a decrease in apparent height of the clusters, which density functional theory (DFT) explains as a restructuring following lattice oxygen reverse spillover.

1. INTRODUCTION

From fine chemical synthesis over combustion control to electrode design – about 80% of industrial chemical processes rely on catalysts to improve energy and material efficiency,¹ of which about 85–90% are catalyzed heterogeneously.² Such a heterogeneous catalyst typically consists of small metal nanoparticles (several 100s to 1000s of atoms) or clusters (often defined as ≤ 100 atoms) dispersed on oxidic support materials.^{3,4} In contrast to the bulk, small clusters exhibit discrete electronic states, comparable to molecules, and therefore develop unique, strongly size-dependent chemical and physical properties. Small Pt clusters, for example, exhibit a non-metallic behavior.⁵ These properties can even change the catalytic behavior: Au, which is inert in the bulk state, becomes highly active and selective for redox catalysis.^{6–8} In small particles, a large proportion of atoms is in direct contact with the underlying support, which can strongly influence their catalytic performance and stability: It can alter the catalytic activity of the particles indirectly,^{9,10} itself be an integral part of the catalytic cycle,¹¹ and even encapsulate the particle in the strong metal support interaction (SMSI),^{12–14} thereby reducing¹⁵ or enhancing¹⁶ the catalytic activity.

In the case of the CO oxidation on supported metal clusters, several reaction mechanisms have been distinguished based on the oxygen supply: When clusters are supported on non-reducible oxides, the CO oxidation typically takes place in a Langmuir-Hinshelwood mechanism, where CO and O₂ co-adsorb from the gas phase and react.^{17,18} On reducible oxide-supported clusters, on the other hand, the support can contribute lattice oxygen in a Mars van Krevelen (MvK) mechanism, thus not only providing a large oxygen reservoir but potentially also causing the entire catalyst system to restructure continuously.^{19,20} The removal of lattice oxygen typically requires thermal activation, which can be facilitated in proximity to the clusters in a so-called metal-assisted MvK

mechanism.²¹ The resulting oxygen vacancies subsequently have to be refilled by gas phase O₂ in order to complete the catalytic cycle. A central question remains whether the oxidation step takes place at the cluster/support boundary or on the cluster. For larger nanoparticles on supports such as ceria^{22,23} and Co₃O₄(111),²⁴ it was demonstrated that the reaction takes place on the particles via an oxygen reverse spillover, *i.e.* lattice oxygen transport onto the particles, which we will thus refer to as “lattice oxygen reverse spillover”. We note that this process is different from the classical reverse spillover, where the partial pressure of the reactants may be increased through adsorption from the gas phase in a capture zone and migration to the catalytic site.²⁵

Here, we study a similar CO oxidation catalyst with two important differences: We use small monodisperse clusters at the extreme low end of the size scale (namely Pt₅ and Pt₁₉) and we deposit them on a magnetite, Fe₃O₄(001), support, where we expect the oxygen exchange to be influenced by a high cation mobility: While oxygen vacancies created on the above-mentioned supports need to be refilled from the gas phase, magnetite can maintain its surface stoichiometry by facile iron diffusion into the bulk,²⁶ and thus provides a flexible oxygen reservoir. Magnetite is a magnetic, abundant, and reducible metal oxide which crystallizes in an inverse spinel structure with Fe²⁺ occupying octahedral sites and Fe³⁺ occupying tetrahedral and octahedral sites in a 1:1 ratio, within an fcc-O²⁻ anion lattice.²⁷⁻²⁹ Its (001) surface reconstructs into the subsurface cation vacancy (SCV) structure, whereby only Fe³⁺ occurs in the uppermost layers, yielding a ($\sqrt{2} \times \sqrt{2}$)R45° reconstruction.³⁰ In the STM, this structure is observed in the form of parallel, undulating rows of iron atoms in octahedral sites, rotated 90° between adjacent terraces. The Fe₃O₄(001) surface is rich in surface defects such as surface hydroxyls, antiphase domain boundaries (APDB) between two reconstruction domains, or Fe-rich point defects such as unreconstructed unit cells and Fe

adatoms.^{31–34} These defects also act as adsorption and dissociation sites, thus participating in the surface chemistry.^{35–37}

In the present work, we combine a multi-modal experimental approach comprising scanning tunneling microscopy (STM), temperature programmed desorption (TPD) as well as highly sensitive pulsed reactivity experiments with state-of-the-art density functional theory (DFT) calculations to investigate a Pt_n/Fe₃O₄(001) model catalyst during exposure to a CO oxidation reaction environment. We demonstrate lattice oxygen reverse spillover onto the small Pt clusters, observe a size dependence of CO poisoning, and identify an oxygen-induced restructuring of the clusters.

2. METHODS

2.1. Experimental Methods

Naturally grown Fe₃O₄(001) samples (SurfaceNet GmbH) were prepared by several preparation cycles, each consisting of 20 min Ar⁺ ion sputtering at room temperature (4×10^{-5} mbar Ar, 1 keV, 3.6 μ A sputter current), followed by annealing in 5×10^{-7} mbar O₂ at 983 K. This procedure yields a reproducible and clean surface, which was checked for stoichiometry as well as carbon impurities using X-ray photoelectron spectroscopy (XPS) and STM on a regular basis. For heating, a boron nitride heater located directly in the sample holder in contact with the sample was used; the temperature was measured by a type K thermocouple directly attached to the crystal.

Size-selected Pt clusters were generated by a laser ablation source.³⁸ Pt is evaporated from a rotating target using the second harmonic of a pulsed Nd:YAG laser; the resulting plasma is subsequently cooled in the adiabatic expansion of a He pulse (Westfalen AG, grade 6.0). This yields a supersonic beam of clusters, which is focused by several electrostatic lenses and guided

towards a 90° quadrupole bender for positive charge selection. The resulting beam is mass-selected by a quadrupole mass filter and subsequently soft-landed on the substrate (i.e. with a kinetic energy < 1 eV/atom). The clusters were deposited at room temperature. For TPD and reactivity measurements, a cluster density of 0.05 clusters /nm² was used, for STM a lower cluster coverage of 0.01 clusters /nm² allowed optimal evaluation of the terrace background around each cluster.

All experiments were carried out under ultrahigh vacuum (UHV) conditions, with a system base pressure of < 1 x 10⁻¹⁰ mbar. All STM measurements were performed in constant current mode with a commercial Omicron VT-SPM instrument using electropolished Pt/Ir tips (Unisoku). STM image processing was performed with Gwyddion³⁹ using plane subtraction and row by row alignment tools for background correction. The height distribution of the particles was determined using a home-written Igor routine by detection of the particles via an intensity threshold, drawing a profile through the cluster maximum and determining the height of the cluster with respect to its surrounding background.

The experimental setup was recently equipped with a device for high sensitivity TPD and reactivity measurements, the so-called sniffer, which was built adapting a design by Bonanni *et al.*⁴⁰ In short, this device combines a pulsed reactant doser with a differentially pumped quadrupole mass spectrometer (Pfeiffer Vacuum GmbH, QMA 200 Prisma Plus). Up to two different reactants can be pulsed independently. The reactants as well as the desorption and reaction products are guided using a heated quartz tube assembly. As the distance between sniffer entrance and sample is typically in the range of only ~100 – 200 μm, the investigated surface is sufficiently decoupled from the rest of the chamber, thus a high amount of reactant can be dosed while keeping UHV conditions in the surrounding chamber. In the present study, each pulse corresponded to a dosage of approximately 0.1 L. This decoupling in combination with the guiding tubes results in the vast

majority of the desorption and reaction products reaching the QMS, yielding a very high sensitivity, as well as the spectra being free of any additional peaks caused by desorption from e.g. the sample holder or the manipulator. The TPD and pulsed reactivity experiments were carried out using O₂ (Westfalen AG, grade 5.0) and C¹⁸O (Eurisotop, 96.1%). All reactivity and TPD-related samples have been saturated with C¹⁸O during cluster deposition. The delay between the pulses during the reactivity measurements was 4 s for O₂, 2.5 s for C¹⁸O, and 2.5 s when pulsing O₂ and C¹⁸O alternatingly. The evaluation of the pulsed reactivity data was carried out using a Matlab-based evaluation tool that differentiates between pulse-related gas signals and background by detecting single peaks and evaluating in a pre-set time window. The thus-determined background comprises offsets, desorption signals, initial pulse valve transients and reactivity linked to long residence times and is subtracted; afterwards each pulse is integrated numerically. For details, see Figure S1 in the Supporting Information (SI).

2.2. Computational models and methods

DFT calculations have been performed to model the lattice oxygen reverse spillover process. To this end, we considered a Pt₅ cluster supported on the Fe₃O₄(001) surface. For the calculations we used the code VASP 5.⁴¹ The core electrons are described with the projector-augmented wave method.^{42,43} O(2s, 2p), Fe(3s, 3p, 3d, 4s) and Pt(5d, 6s) electrons are treated explicitly. Spin-polarized calculations are carried out at the level of the Generalized Gradient Approximation (GGA) adopting the Perdew, Burke and Ernzerhof PBE exchange-correlation functional.⁴⁴ The strongly correlated character of Fe(3d) electrons is accounted for as in the GGA+U approach^{45,46} by applying a Hubbard U parameter of 3.8 eV to the Fe 3d states.³⁰ The magnetic structure of Fe₃O₄ is correctly reproduced. Long-range dispersion is included according to the D3 method introduced by Grimme.⁴⁷ The relaxation of the magnetite bulk lattice parameters and internal coordinates has

been performed with a 3x3x3 K-points grid and a kinetic energy cutoff of 600 eV. All subsequent calculations on the (001) surface have then been carried out with a 2x2x1 K-points grid and a kinetic energy cutoff of 400 eV. The calculations on gas phase Pt clusters are carried out in Γ point only in a cubic 25 Å box. The truncation criteria for the electronic and ionic loops are 10^{-5} eV and 10^{-2} eV/Å, respectively. Kinetic barriers are calculated according to the Climbing Image-Nudged Elastic Band approach,⁴⁸ considering four images along the reaction path.

The (001) surface of the magnetite is modelled by a $(\sqrt{2} \times \sqrt{2})R45^\circ$ Fe₃₅O₄₈ slab, according to the subsurface-vacancy model formerly proposed by Parkinson and co-workers.³⁰ Further details on the model structures are reported in Section S2 of the SI.

To model the formation of an O vacancy, we distinguish three non-equivalent oxygen lattice positions on the Fe₃O₄(001) surface. O1 and O2 lie on threefold-coordinated surface sites connecting Fe atoms in tetrahedral positions. O3 lies on top of an Fe ion in an octahedral site (see Figure S4). The thermodynamic stability of the O vacancy (estimated with respect to the pristine surface and $\frac{1}{2}$ O₂) depends on the site where the oxygen atom is removed. In particular, O3 located on top of Fe ions in octahedral sites can be removed at a cost of 2.91 eV; removal of O2 (3.10 eV) and O3 (3.55 eV) requires more energy (see also SI, Section S3).

3. RESULTS AND DISCUSSION

In order to identify how CO binds to Pt_n/Fe₃O₄(001) and whether it reacts with lattice oxygen, we start with a discussion of the TPD spectra of CO-saturated surfaces without external oxygen supply. Subsequently, the reactivity linked with either the CO or O₂ reactant is monitored by pulsed reactivity measurements. A low temperature reaction peak demonstrates that the lattice oxygen reverse spillover leads to a highly reactive oxygen species on the cluster. Finally, we will show

that the lattice oxygen reverse spillover leads to structural changes of the clusters. We should note at this point that over the entire temperature range discussed below, STM indicates the cluster coverage remains constant and the distribution monodisperse. In the following, ripening can thus be excluded from the discussion.

3.1. Setting the stage: CO oxidation in TPD measurements

Figure 1(a) shows CO desorption curves from Pt₅ (orange) and Pt₁₉ clusters (gray) deposited onto the Fe₃O₄(001) surface. First, Pt₁₉ clusters exhibit a broad desorption feature with an onset temperature of around 350 K and a peak temperature of 475 K. This feature is not observed on the bare magnetite surface (see Figure S5 in the SI), agrees with the temperature range reported for CO desorption from Pt nanoparticles on Fe₃O₄(001),⁴⁹ and can therefore be assigned to the clusters. Second, the weak and broad feature with a maximum at 710 K is similar to the CO recombinative desorption from Fe(111).⁵⁰ We thus conclude that it results from CO which has been adsorbed dissociatively on the small number of highly reduced iron sites, most likely Fe adatoms, which are a common defect on the Fe₃O₄(001) surface.³¹ Finally, there is another small feature around 330 K. Such features have been tentatively assigned in literature to reduced iron sites that surround Pt nanoparticles on Fe₃O₄(111), when strong metal support interaction sets in.⁵¹ While this interaction requires higher temperatures not yet reached here, there could already be clusters present in close proximity to reduced iron defects.

The CO desorption features of Pt₅ are comparable to those of Pt₁₉, with the difference that the desorption maxima are shifted to higher temperatures, indicating stronger binding. Note that all Pt₅ measurements end at 625 K, as cluster ripening was observed in STM when heating to higher temperatures (see Figure S6). The main CO desorption feature from Pt₅ with an onset around 420 K

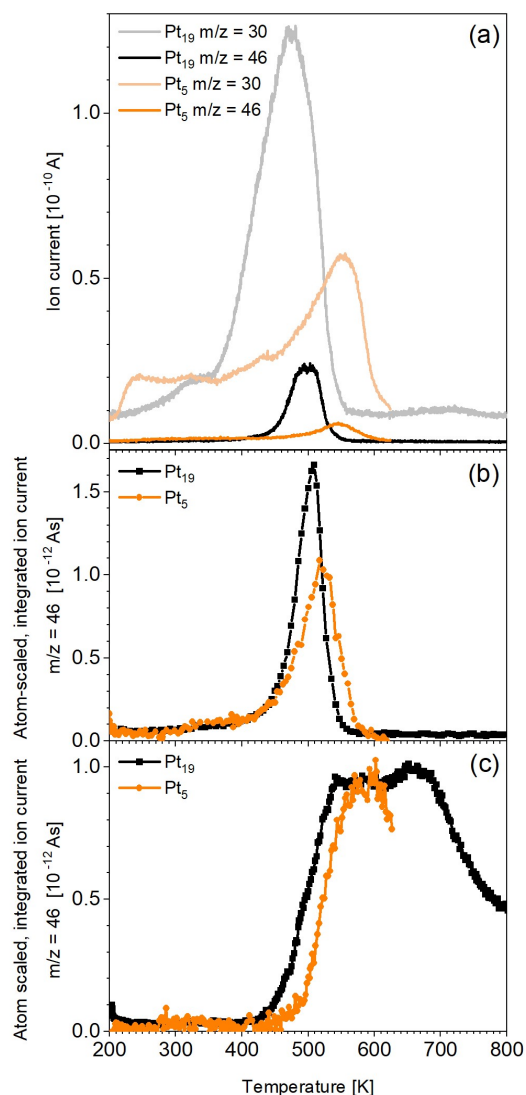


Figure 1. TPD and pulsed reactivity spectra of Pt₁₉ (black, grey) and Pt₅ (orange) supported on Fe₃O₄(001). By using the same cluster density of 0.05 clusters/nm², the resulting atom density is ~4 times higher for the Pt₁₉ sample. (a) Saturation TPD curves of C¹⁸O adsorbed at 200 K. The C¹⁸O (m/z = 30) and C¹⁸O¹⁶O (m/z = 46) traces are shown. (b) C¹⁸O¹⁶O (m/z = 46) production as a function of the temperature, synchronized with O₂ reactant pulses on C¹⁸O-saturated samples. (c) C¹⁸O¹⁶O (m/z = 46) formation synchronized with C¹⁸O reactant pulses on C¹⁸O-saturated samples. The heating rate was 1 K/s. All pulsed data were integrated and normalized to the Pt atom coverage.

and a peak at 550 K is assigned to the clusters. A lower temperature feature at around 430 K is observed, comparable to the one observed at 330 K for Pt₁₉. For both cluster sizes, this feature is located around the onset temperature of the main desorption peak, i.e. both features are shifted similarly. This might indicate a similar origin of the lower temperature feature, namely due to clusters in the vicinity of reduced surface defect sites.

In both samples, we observe weak desorption signals in the temperature range < 300 K, which we assign to desorption from defects in the magnetite support (see TPD for bare magnetite in Figure S5).³⁵ Since their intensity decreases upon cluster deposition, we conclude that a significant part of the clusters is most likely located on surface defect sites such as unreconstructed unit cells or antiphase domain boundaries.^{31,52} Note that the background at these low temperatures varies with the state of the single crystal which we suspect is due to slight changes in sample cleanliness, oxidation state and/or defect density. The measurements comparing bare and cluster-covered magnetite were therefore recorded in close temporal sequence.

Having understood the CO features, we can now interpret the C¹⁸O¹⁶O production signals recorded simultaneously with the CO desorption (also shown in Figure 1(a)). Since no oxygen is dosed, this CO₂ production, observed for both cluster sizes, must be strictly related to the availability of lattice oxygen for reaction with CO. During the TPD measurements, only C¹⁸O¹⁶O and no C¹⁸O₂ is observed, excluding a Boudouard-type reaction ($2 \text{ CO} \rightarrow \text{C} + \text{CO}_2$). We are thus observing a MvK reaction. For Pt₁₉, the CO₂ feature has an onset temperature located around 400 K and a broad peak at 500 K. Pt₅ exhibits a similar feature, starting below 420 K with the peak at 545 K. Note that we observe a change in apparent cluster height in the same temperature range in STM measurements, as will be discussed later. As no CO₂ desorption could be detected for the bare Fe₃O₄(001) surface (see Figure S5), we attribute the CO₂ signals to the presence of the clusters. For both cluster sizes,

they exhibit about the same onset temperature and peak position with respect to the corresponding CO desorption peaks, indicating that the CO₂ formation is closely related to the CO desorption.

3.2. Exploring the reaction mechanism by overcoming reactant limitations: Pulsed-reactivity measurements

Complementary to the TPD experiments, we performed pulsed valve experiments that give access to the reaction rate synchronized with a given reactant pulse. In these background-corrected measurements (see Section S1), each data point is the integral over a product pulse and correlates with the reaction rate at a given temperature. These reactant-synchronized pulsed measurements allow us to investigate adsorption limitations, (i) of oxygen adsorption by CO poisoning (in pulsed O₂ experiments) and (ii) of CO adsorption at high temperatures (in pulsed CO experiments).

We start with pulsing O₂ onto the CO pre-covered sample and observe the CO₂ production shown in Figure 1(b) for Pt₅ (orange) and Pt₁₉ clusters (black). The CO₂ formation starts around 400 K for both cluster sizes and peaks at 505 K for Pt₁₉ and 520 K for Pt₅, respectively. This difference reflects the slightly higher binding energy of CO on Pt₅. While the cluster surface is poisoned with CO at low temperatures, binding sites for dissociative O₂ adsorption become available above the onset temperature of CO desorption, leading to co-adsorption of oxygen and CO on the same cluster.¹⁸ At this temperature, the CO oxidation in a classical Langmuir-Hinshelwood fashion is already facile on clusters⁵³ and hence a high reaction rate is observed as soon as the adsorption limitations are overcome. The similarity to the CO₂ production in the TPD indicates that it is adsorption-limited as well. As we will discuss in detail in Section 3.5, DFT confirms that the activation barrier for the initial lattice oxygen reverse spillover is below 1 eV, hence far less than the CO binding energy calculated e.g. for Pt₂ clusters on Fe₃O₄(001).⁵⁴

We note that the CO₂ production peak on Pt₅ in the pulsed experiments is at a somewhat lower temperature than the peak observed in TPD, contrary to Pt₁₉. This observation can be explained by a reaction limitation due to a lack of CO which is not replenished during the measurement. When supplying CO by alternating CO and O₂ pulses (see Figure S7), the CO₂ formation synchronized with the O₂ pulses follows the shape of the corresponding CO₂ TPD trace, with the same onset and peak temperatures, thus confirming the hypothesis above.

We now describe the opposite experiment, pulsing CO without providing any oxygen. Figure 1(c) shows the CO₂ production observed for both investigated cluster sizes as a function of temperature. For Pt₁₉, CO₂ formation starts at around 425 K, reaching a plateau between 550 K and 670 K with approximately constant CO₂ formation rate. On Pt₅, an onset temperature of 450 K is observed, with a maximum at 590 K. This experiment allows to probe the behavior of the CO₂ formation over a wider temperature range, since the reactant is refreshed continuously by pulses and thus also available beyond the CO desorption temperature. As expected, the CO₂ production starts at the onset temperature of CO₂ formation in the TPD experiment, for both cluster sizes, although at a slightly higher temperature, where oxygen migration onto the cluster is no longer hindered by CO. The signal saturates once all available cluster sites can accommodate active oxygen atoms. This temperature coincides with the temperature where CO desorption is complete. Interestingly, the normalized peak intensity is the same for both cluster sizes. The number of active sites hence scales with the surface and not the rim of the cluster.¹ The upper limit of the plateau could be due

¹ The intensity shown in Figure 1 (c) is normalized to the number of Pt atoms per cluster. Taking the average cluster heights at ≥ 450 K from our STM measurements (see Section 3.4) into account for a conservative geometrical estimate, we can estimate the number of atoms at the rim and on the surface of the clusters and normalize them to the number of cluster atoms: Pt₅ is a single layer cluster with 5 (normalized 1) rim atoms and 5 (normalized 1) surface atoms (see Figure 4(c)) and Pt₁₉ a bilayer cluster with ~ 9 (normalized 0.5) rim and ~ 16 (normalized 0.8) surface atoms,

to encapsulation effects or due to limited oxygen coverage: chemisorption on stepped Pt(112) leads to O₂ desorption just below 700 K.⁵⁵ All the plateau characteristics point to a reaction that is limited by free adsorption sites on the cluster surface and that proceeds *on* the cluster, via lattice oxygen reverse spillover. In contrast, an interface reaction would not saturate as long as CO (and lattice oxygen) are available since the two reactants do not compete for adsorption sites.

3.3. Lattice oxygen reverse spillover in sequential CO TPDs

Having shown the ease of lattice oxygen reverse spillover once adsorption sites are available, we now use this highly active oxygen species in a low temperature reaction. We know from literature that the CO oxidation on Pt clusters after sequential adsorption of oxygen and CO already takes place below 400 K.^{18,53}

In the experiment in Figure 2, we show that it is indeed possible to observe an additional CO₂ production feature when populating the clusters with oxygen by reverse spillover prior to CO adsorption. Figure 2 shows a sequence of CO₂ production TPD curves on a Pt₅ sample, each taken after saturating the surface with CO at 200 K. Remarkably, the anticipated low-temperature CO₂ feature around 300-370 K is observed only for one out of four runs, the second one. While CO poisoning and an activation barrier hinder oxygen migration onto the cluster in the first run, the second run starts already with a certain oxygen coverage on the clusters, built up from lattice oxygen during the first temperature ramp. This reaction is, however, not repeated in the third and fourth run, where another effect comes into play that is clearly reflected in the intensity loss of the primary CO₂ production peak: At the high temperature end of the TPD, cluster encapsulation due

respectively. The number of active sites hence scales with the surface and not the rim of the cluster as we see similar activities per cluster atom.

to SMSI starts, an effect that strongly affects the cluster reactivity, as studied for nanoparticles,⁴⁹ while requiring further investigation for clusters. Here, it leads to the well-known loss of CO adsorption capability that we see in an independent series of CO TPDs (see Figure S8). Since the encapsulation is incomplete after the first run, but finished after the second, we no longer observe the facilitated low-temperature CO₂ production thereafter. Note that the low intensity of this CO₂ production feature is likely caused by partial encapsulation after the first ramp. Summing up, this experiment provides direct proof for reverse spillover of lattice oxygen.

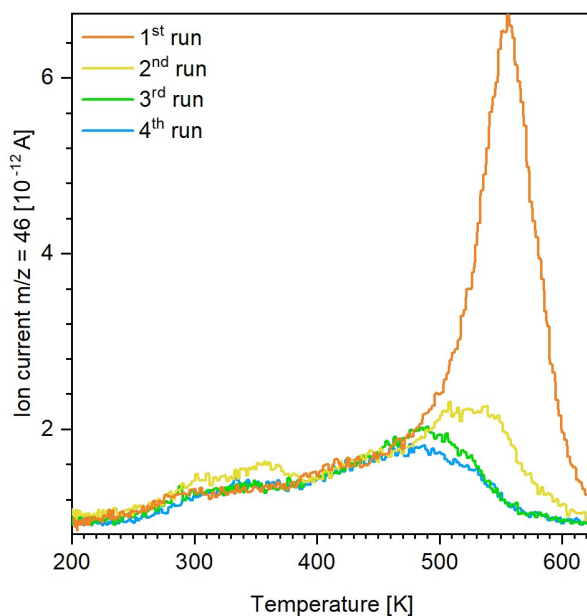


Figure 2. C¹⁸O¹⁶O (m/z = 46) formation in subsequent CO-TPD spectra of Pt₅ supported on Fe₃O₄(001). In each run, the surface is saturated with C¹⁸O at 200 K; the heating rate was 1 K/s. Only in the second run (yellow), a CO₂ production feature around 300-370 K is observed. The main feature above 500 K decreases during the first two runs. Figure S8 shows the corresponding C¹⁸O desorption signals.

3.4. Effects of the lattice oxygen reverse spillover on cluster structure: STM measurements

In the following, we focus on the effects of this lattice oxygen reverse spillover on the cluster structure, concerning geometry and electronic state. Figure 3(a–e) shows a series of STM images displaying Pt₁₉ clusters on a defect-rich Fe₃O₄(001) surface, recorded at the temperatures indicated in the Figure. The clusters appear as bright protrusions on the surface and seem to be largely randomly distributed while maintaining their size upon deposition. At all temperatures investigated here, the clusters are still monodisperse; ripening or disintegration is not observed. At 473 K and even more pronounced at 573 K, tiny holes form around some of the clusters, but not all (details see Figure S9). Such holes are typically observed on this surface when oxygen atoms are removed, leaving behind undercoordinated iron atoms that diffuse into the bulk.²⁰ This is a direct consequence of the lattice oxygen reverse spillover occurring around the clusters. The hole formation is more or less pronounced depending on the amount of CO in the chamber background that reacts off oxygen from the clusters, creating free adsorption sites for renewed oxygen migration.

Upon annealing, the cluster brightness seems to decrease, indicating a decline in their apparent height, while the coverage remains constant (confirmed by statistical analysis of several images of the same sample at different temperatures). This finding is quantified in Figure 3(f) for Pt₁₉ where the cluster height distributions at different temperatures are presented in histograms. Dashed red lines are used to indicate the approximate correspondence to atomic layers. While the Pt₁₉ clusters are about three atomic layers high at room temperature, they flatten to between one and two layers at 573 K. The transition takes place between 423 K and 523 K, which is the temperature range where CO₂ formation is observed in Figure 1(a). This strong correlation in temperature suggests that the change in apparent height is caused by lattice oxygen reverse spillover.

When comparing several cluster sizes in Figure 3(g), we find that this is a general phenomenon. The decrease in height holds for all investigated cluster sizes, suggesting the lattice oxygen reverse spillover to be a universal effect for the $\text{Pt}_n/\text{Fe}_3\text{O}_4(001)$ system. Such a behavior could either be explained by a real geometry change of the clusters or by a change in the density of states due to oxygen adsorption.

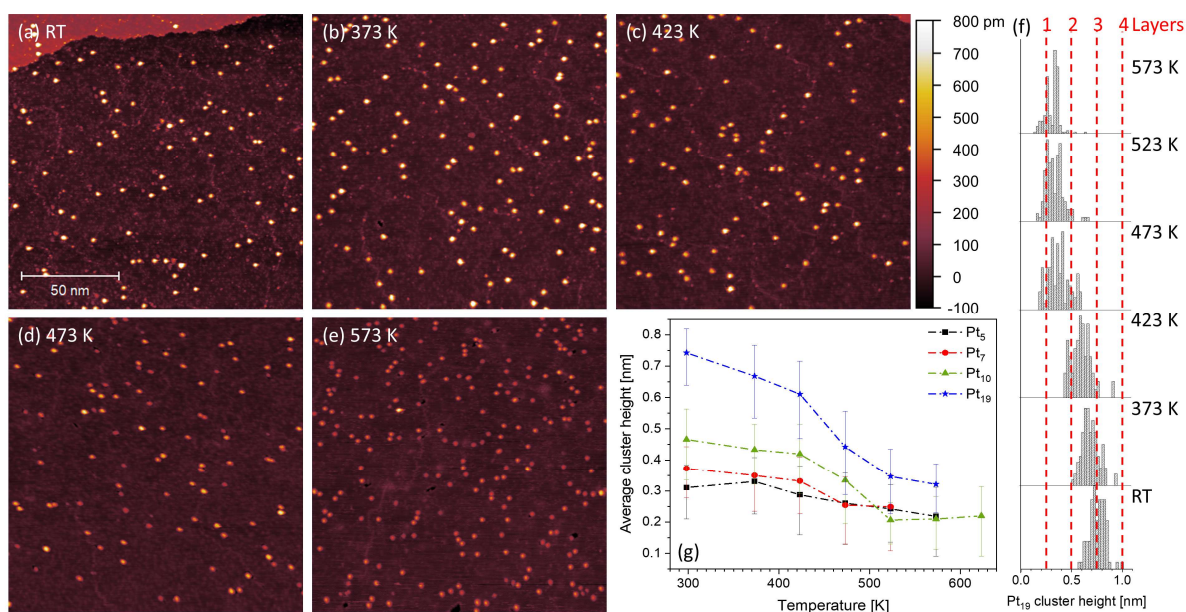


Figure 3. Height evolution of $\text{Pt}_n/\text{Fe}_3\text{O}_4(001)$ as a function of temperature. (a)–(e) STM images ($150 \times 150 \text{ nm}^2$) of Pt_{19} clusters ($0.01 \text{ clusters/nm}^2$) measured at the temperatures indicated. All images have been scaled to the same false color scale for height comparison.² (f) Height profiles comparing the size distribution of Pt_{19} in (a)–(e) as a function of temperature. (g) Evolution of the average cluster height as a function of temperature for Pt_5 , Pt_7 , Pt_{10} and Pt_{19} . *Imaging parameters:* $V_b = 1.50 \text{ V}$; (a, e) $I_t = 300 \text{ pA}$, (b, c, d) $I_t = 400 \text{ pA}$.

² Note that (e) is from a second set of experiments with a slightly higher cluster coverage than (a)–(d). The coverage in (e) is consistent with the coverage of the same sample after RT deposition.

3.5. DFT calculations reveal further mechanistic details

The experimental results point to some mechanistic aspects that require theoretical investigation. In particular, we consider the following questions: (i) How easy is it to remove lattice oxygen from bare magnetite vs. in the vicinity of a cluster? (ii) Is lattice oxygen reverse spillover endo- or exothermic and can we confirm that the clusters can be covered by considerable amounts of oxygen? (iii) What is the activation barrier? (iv) Can the apparent height change in STM be explained by a restructuring?

First, we studied the structure of a gas phase Pt₅ cluster, starting from the most stable isomers reported in the literature.⁵⁶⁻⁶² This led to six isomers with very similar stability; the energy difference between the ground state and the least stable of the six isomers considered here is 0.35 eV, and sometimes different structures are separated by a few meV, suggesting a fluxional behavior of the gas phase clusters (see SI, Section S9). Upon deposition on Fe₃O₄, some of the structures retain the topology of the gas phase, while others undergo a strong rearrangement. The Pt₅ adsorption energies (Table S4), computed with respect to Fe₃O₄(001) and the most stable Pt₅ isomer (Pt₅(i) in Figure S10), show that the ground state corresponds to a capped rhombus, with an adsorption energy of -4.51 eV, shown in Figure 4(a), followed by a square pyramidal Pt₅ cluster (Figure 4(b)) and a planar structure (Figure 4(c)). Note that the most stable isomer, Figure 4(a), is 1.5 eV more favorable than the next one, which shows that the surface has a strong stabilizing effect on this structure. This also suggests that the conversion of one isomer into another is much more difficult than in the gas phase.

Upon deposition, the Pt cluster becomes slightly positively charged (by 0.3 e) and a partial quenching of the magnetic moment of the support occurs, with a reduction from 3.3 μ_B per Fe₃O₄ formula unit in the clean surface, to 2.59 μ_B when Pt₅ is adsorbed, as shown in Table S4.

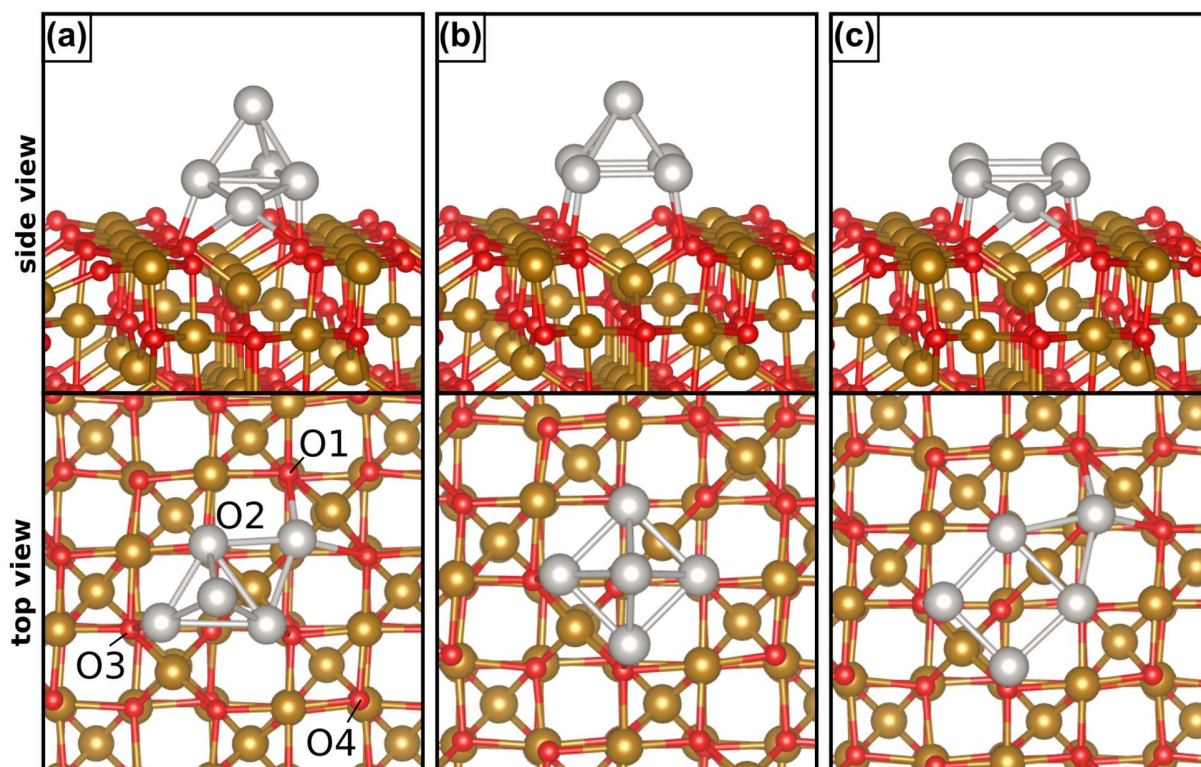


Figure 4. Pt₅ clusters on the Fe₃O₄(001) surface. (a), (b) and (c) are the three most stable isomers, with isomer (a) being 1.5 eV and 1.78 eV lower in energy than the isomers in (b) and (c), respectively. Red, brown, and grey spheres correspond to O, Fe and Pt atoms, respectively.

We now start addressing question (i). The formation energy of an O vacancy on the clean Fe₃O₄(001) surface is about 3 eV (see Table S2 and Section S3). The formation of a metal/oxide interface may facilitate the removal of the O atoms in contact to the metal adduct.²¹ We have explored this possibility by removing O atoms from four possible sites, indicated in Figure 4(a), involving O either in direct contact with Pt₅, or at some distance. The formation energy of an O vacancy on Pt₅/Fe₃O₄ is reduced with respect to the clean surface. In particular, the formation of V_{O2} has a cost of 1.98 eV, about 0.9 eV smaller than the most favorable case on the clean surface, which costs 2.91 eV. Also, the removal of an O atom not in direct contact with Pt₅ (such as V_{O4}) is

slightly easier by almost 0.5 eV (see also SI, Section S10). These results point to a metal-assisted MvK mechanism.

In a second step, we address question (ii) regarding the endo-/exothermicity of the reverse spillover. The mechanism of lattice oxygen reverse spillover involves the displacement of O atoms from the lattice positions and their adsorption on the supported metal cluster. To model this process, we have started from the most favorable case of O removal (V_{O_2} in Figure 4(a)) and have re-adsorbed an O atom on various sites of Pt_5 . A preliminary exploration of O adsorption on gas phase Pt_5 provides information about the most stable adsorption sites (see Table S3). O adsorbs preferentially in a bridge mode or as a terminal Pt-O group, followed by threefold hollow sites. When the cluster is adsorbed on Fe_3O_4 , other adsorption sites are present at the Pt_5/Fe_3O_4 interface. In some cases, the lattice oxygen reverse spillover process is endothermic, but there are also structures where the product is more stable than the initial configuration. The most favorable case is shown in Figure 5(a), where an O from the interface is inserted into a Pt-Pt bond, which is preferred by -0.40 eV (see Table S6 and Figure S11 for further details). Thus, lattice oxygen reverse spillover involving a single O atom is thermodynamically favorable.

This leads us to question (iii) where we want to connect the lattice oxygen vacancy formation with the oxygen adsorption on the cluster by a viable path. This process is activated and the kinetic barrier has been estimated for the initial step of the reaction, i.e. the displacement of an O atom from an O_2 lattice site (see Figure 4(a)) to a nearby interfacial site where it binds at the cluster/magnetite interface, shown in Figure 5. For this specific path, the whole process is almost thermoneutral, and the barrier of 0.93 eV can be overcome by thermal effects at the temperatures involved in the experiments described above. It is reasonable to assume that the displacement of the O atom from the lattice is the rate-determining step of the whole process: further diffusion of

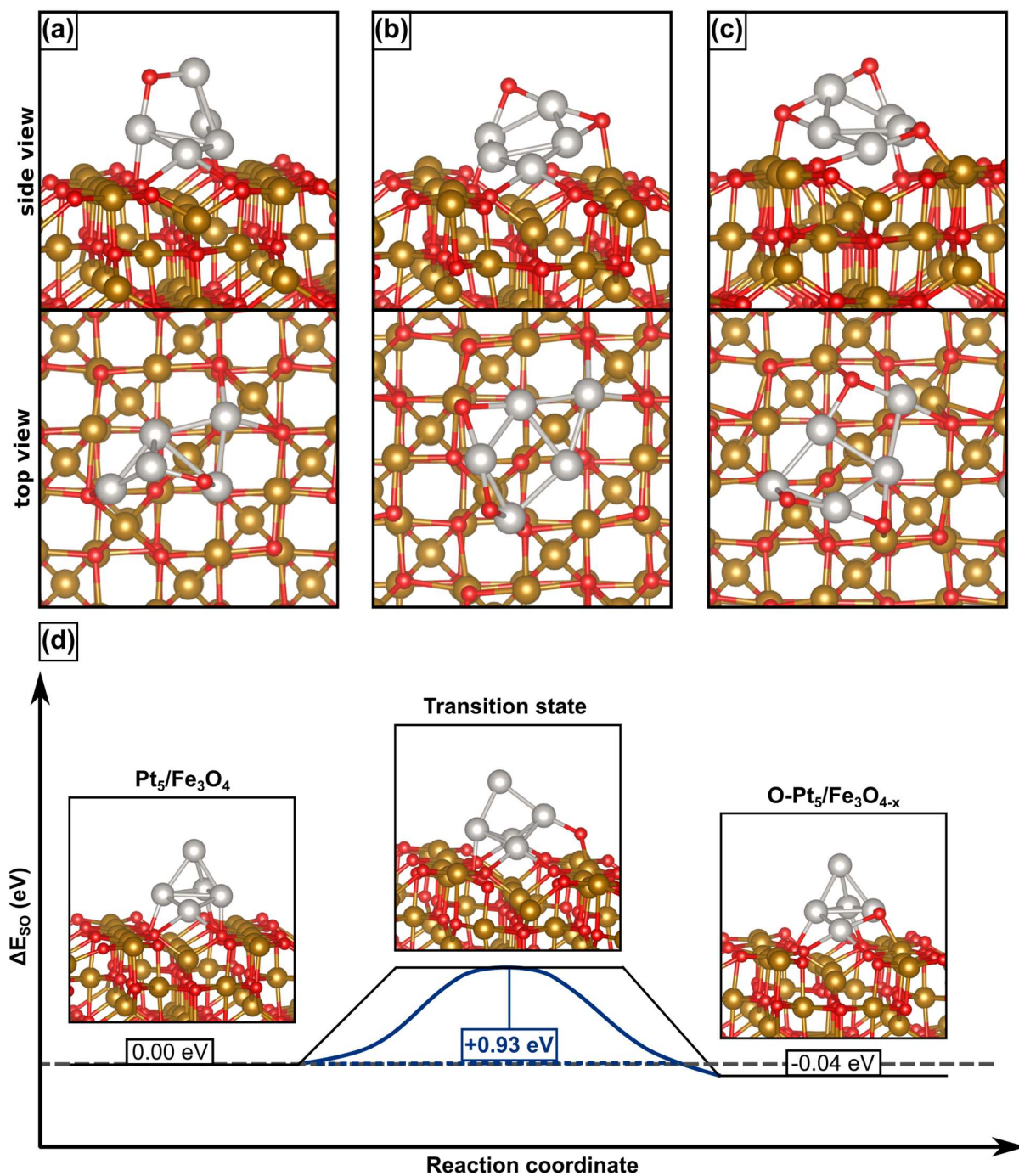


Figure 5. Side and top views of the most stable structures obtained for reverse spillover of (a) one, (b) two, and (c) three lattice oxygen atoms. In (d) the energy profile to displace an O atom from a lattice position to Pt₅ is shown.

O-species on Pt₅ should occur with low barriers due to similar bond strengths of various adsorption sites.

Next, we have considered the case of the removal of a second O atom from various lattice sites and its re-adsorption on Pt₅O. Also in this case, we found a few structures where the process is exothermic. The formation of the most stable isomer, shown in Figure 5(b), where two O atoms are adsorbed on a bridge site, is exothermic by -0.64 eV (see also Table S7 and Figure S12). Finally, the process has also been considered for a third O atom which is removed from the cluster/oxide interface and re-adsorbed on Pt₅, forming an oxidized Pt₅O₃ supported cluster, as shown in Figure 5(c). This generates a large number of possible initial combinations, and we could explore only a few of them. In the most favorable case (Figure 5(c)), the transfer of three O atoms is slightly endothermic, by 0.17 eV only. We cannot exclude the existence of even more favorable isomers, but this already supports the evidence that multiple lattice oxygen reverse spillover from magnetite onto a Pt cluster is energetically accessible (for further details see Figures S11, S12 and Tables S7, S8).

This opens the question of the best channel for CO oxidation, via CO reaction with an O atom of Fe₃O₄ at the rim of Pt₅ or with the O atoms adsorbed on the Pt cluster. The experiments show a complex behavior as a function of CO poisoning, reaction temperature, cluster size, etc. With our simplified models, we compared the energy required to remove oxygen from the Pt₅/Fe₃O₄ interface or from the oxidized Pt₅ cluster. For Pt₅/Fe₃O₄, the removal of one O atom in contact with the cluster costs 2.0, 2.5, 2.7 and 3.1 eV, depending on the site (on average 2.6 eV). These numbers can be compared to the cost of desorbing an O atom from Pt₅O supported on Fe₃O_{4-x} where an O vacancy has been created. In the most stable configuration, this cost is 2.4 eV, indicating that the Pt-O bond is strong and that at low O coverage, removing the O ad-atoms from a Pt cluster has a

comparable cost to removing O atoms at the cluster/oxide interface. Things change for higher O coverages though. We have removed each of the three O atoms from the $\text{Pt}_5\text{O}_3/\text{Fe}_3\text{O}_{4-3x}$ system, and the cost is 1.7, 2.2, and 2.2 eV, respectively (on average 2.05 eV). This suggests that for more pronounced lattice oxygen reverse spillover, or higher O coverages on Pt clusters, the reaction of CO with adsorbed oxygen becomes preferred.

Finally, in question (iv), we want to rationalize the structural changes observed in the STM images. Lattice oxygen reverse spillover indeed induces a structural change in the supported cluster, as apparent in Figures 4 and 5. In particular, there is a tendency to rearrange the structure of Pt_5 from 3D to a quasi-2D as the O loading increases. To quantify this effect, we have computed the average cluster height with respect to the Fe_3O_4 surface for all the cases discussed here, and indeed there is an overall reduction of the cluster height (see SI, Section S12). This could indicate that the height evolution observed in STM, as shown in Figure 3, is due to geometry changes and not purely an electronic effect. However, more work is necessary to confirm this conclusion.

Furthermore, Fe spillover from Fe_3O_4 onto Pt_5 and Pt_5O_3 has been considered, following a similar strategy as described above for lattice oxygen reverse spillover. In all cases considered, however, Fe reverse spillover is highly unfavorable (see SI, Section S13). Thus, if Fe diffusion occurs, this will be towards the bulk of magnetite, not towards the supported Pt clusters. These results suggest that the encapsulation of Pt clusters due to SMSI effects follows more complex paths than the diffusion of isolated Fe atoms.

4. CONCLUSIONS

A central question concerning cluster catalysis with lattice oxygen, in a Mars van Krevelen mechanism, is whether the reaction occurs at the cluster-support rim or on the cluster. We studied

this distinction on the example of metal-assisted MvK in the CO oxidation on small, size-selected Pt_n clusters supported on magnetite Fe₃O₄(001) in a multi-modal experiment, supported by DFT calculations. The detailed TPD and pulsed reactivity experiments revealed a reaction on the cluster that involves reverse spillover of lattice oxygen, a phenomenon hitherto unknown on this support. Via annealing-induced migration, lattice oxygen can be accumulated on the clusters and react in a low temperature window of 300–370 K.

As our calculations for Pt₅ clusters showed, this reverse spillover process is exothermic for the first two oxygen atoms, with an initial migration activation barrier below 1 eV, much lower than the CO desorption barrier. Thus, the lattice oxygen reverse spillover is driven by overcoming CO poisoning and scales with the availability of free adsorption sites. The maximum obtainable turnover rates observed in the pulsed reactivity experiments scale with the number of cluster surface atoms.

STM investigations showed that the clusters remain monodisperse throughout all experiments, but with a distinct decrease in apparent height, concomitant to the formation of holes due to lattice oxygen removal. The calculations suggest that this change could be due to a true geometrical adaptation upon lattice oxygen reverse spillover resulting in a transition from 3D to 2D clusters.

Larger Pt nanoparticles on the same support have been shown to become encapsulated by a thin, reduced iron oxide film due to SMSI.⁴⁹ In first experiments we found this effect to also occur on small clusters, at temperatures where lattice oxygen reverse spillover already occurred. Calculations suggest that the growth of thin oxide films occurs through more complex paths than the diffusion of isolated Fe atoms, warranting more extensive future investigations.

Supporting Information. S1. Pulsed reactivity data evaluation. S2. Characterization of magnetite bulk and (001) surface by DFT calculations. S3. Formation of a surface oxygen vacancy on various sites. S4. CO desorption from bare magnetite and magnetite-supported clusters in TPD. S5. Ripening of Pt₅ in STM. S6. Alternating CO and O₂ pulses on Pt₅/Fe₃O₄(001). S7. Loss of CO adsorption capability upon cluster encapsulation. S8. Hole formation in cluster vicinity. S9. Platinum clusters in the gas phase: structure relaxation and oxygen adsorption. S10. Adsorption of Pt₅ on Fe₃O₄(001) and formation of oxygen vacancies. S11. Lattice oxygen reverse spillover. S12. Impact of lattice oxygen reverse spillover on cluster height. S13. Iron spillover.

ACKNOWLEDGEMENTS

The experimental work was funded by the Deutsche Forschungsgemeinschaft (DFG, German Research Foundation) under Germany's Excellence Strategy – EXC 2089/1 – 390776260 and project numbers ES 349/5-2 and HE 3454/23-2. This project has received funding from the European Research Council (ERC) under the European Union's Horizon 2020 research and innovation programme (grant agreement No 850764). B.A.J.L. gratefully acknowledges financial support from the Young Academy of the Bavarian Academy of Sciences and Humanities. F.M., S.T. and G.P. acknowledge support from the Italian Ministry of University and Research (MIUR) through the PRIN Project 20179337R7, the grant Dipartimenti di Eccellenza - 2017 "Materials For Energy", and the CINECA supercomputing center via ISCRAB.

ORCID

Barbara A. J. Lechner: 0000-0001-9974-1738

Ueli Heiz: 0000-0002-9403-1486

Gianfranco Pacchioni: 0000-0002-4749-0751

Friedrich Esch: 0000-0001-7793-3341

REFERENCES

- (1) Ma, Z.; Zaera, F. Heterogeneous Catalysis by Metals. In *Encyclopedia of Inorganic Chemistry*; John Wiley & Sons, Ltd: Chichester, United Kingdom, **2006**.
- (2) Chorkendorff, I.; Niemantsverdriet, J. W. *Concepts of Modern Catalysis and Kinetics*; John Wiley & Sons, **2017**.
- (3) Bell, A. T. The Impact of Nanoscience in Heterogeneous Catalysis. *Science* **2003**, *299* (5613), 1688–1691.
- (4) Schauermaun, S.; Nilius, N.; Shaikhutdinov, S.; Freund, H. J. Nanoparticles for Heterogeneous Catalysis: New Mechanistic Insights. *Acc. Chem. Res.* **2013**, *46* (8), 1673–1681.
- (5) Eberhardt, W.; Fayet, P.; Cox, D. M.; Fu, Z.; Kaldor, A.; Sherwood, R.; Sondericker, D. Photoemission from Mass-Selected Monodispersed Pt Clusters. *Phys. Rev. Lett.* **1990**, *64* (7), 780–783.
- (6) Valden, M.; Lai, X.; Goodman, D. W. Onset of Catalytic Activity of Gold Clusters on Titania with the Appearance of Nonmetallic Properties. *Science* **1998**, *281* (5383), 1647–1650.
- (7) Sanchez, A.; Abbet, S.; Heiz, U.; Schneider, W.-D.; Häkkinen, H.; Barnett, R. N.; Landman, U. When Gold Is Not Noble: Nanoscale Gold Catalysts. *J. Phys. Chem. A* **1999**, *103* (48), 9573–9578.
- (8) Bus, E.; Prins, R.; van Bokhoven, J. A. Origin of the Cluster-Size Effect in the Hydrogenation of Cinnamaldehyde over Supported Au Catalysts. *Catal. Commun.* **2007**, *8*

- (9), 1397–1402.
- (9) Crampton, A. S.; Rotzer, M. D.; Landman, U.; Heiz, U. Can Support Acidity Predict Sub-Nanometer Catalyst Activity Trends? *ACS Catal.* **2017**, *7* (10), 6738–6744.
- (10) Lee, S.; Lee, B.; Seifert, S.; Winans, R. E.; Vajda, S. Fischer-Tropsch Synthesis at a Low Pressure on Subnanometer Cobalt Oxide Clusters: The Effect of Cluster Size and Support on Activity and Selectivity. *J. Phys. Chem. C* **2015**, *119* (20), 11210–11216.
- (11) Walenta, C. A.; Kollmannsberger, S. L.; Courtois, C.; Pereira, R. N.; Stutzmann, M.; Tschurl, M.; Heiz, U. Why Co-Catalyst-Loaded Rutile Facilitates Photocatalytic Hydrogen Evolution. *Phys. Chem. Chem. Phys.* **2019**, *21* (3), 1491–1496.
- (12) Tauster, S. J. Strong Metal-Support Interactions. *Acc. Chem. Res.* **1987**, *20* (11), 389–394.
- (13) Dulub, O.; Hebenstreit, W.; Diebold, U. Imaging Cluster Surfaces with Atomic Resolution: The Strong Metal-Support Interaction State of Pt Supported on TiO₂(110). *Phys. Rev. Lett.* **2000**, *84* (16), 3646–3649.
- (14) Qin, Z. H.; Lewandowski, M.; Sun, Y. N.; Shaikhutdinov, S.; Freund, H. J. Encapsulation of Pt Nanoparticles as a Result of Strong Metal-Support Interaction with Fe₃O₄ (111). *J. Phys. Chem. C* **2008**, *112* (27), 10209–10213.
- (15) Polo-Garzon, F.; Blum, T. F.; Bao, Z.; Wang, K.; Fung, V.; Huang, Z.; Bickel, E. E.; Jiang, D.; Chi, M.; Wu, Z. In Situ Strong Metal–Support Interaction (SMSI) Affects Catalytic Alcohol Conversion. *ACS Catal.* **2021**, *11* (4), 1938–1945.
- (16) Lewandowski, M.; Sun, Y. N.; Qin, Z. H.; Shaikhutdinov, S.; Freund, H. J. Promotional Effect of Metal Encapsulation on Reactivity of Iron Oxide Supported Pt Catalysts. *Appl.*

- Catal. A Gen.* **2011**, *391* (1–2), 407–410.
- (17) Kunz, S.; Schweinberger, F. F.; Habibpour, V.; Röttgen, M.; Harding, C.; Arenz, M.; Heiz, U. Temperature Dependent CO Oxidation Mechanisms on Size-Selected Clusters. *J. Phys. Chem. C* **2010**, *114* (3), 1651–1654.
- (18) Heiz, U.; Sanchez, A.; Abbet, S.; Schneider, W. D. Catalytic Oxidation of Carbon Monoxide on Monodispersed Platinum Clusters: Each Atom Counts. *J. Am. Chem. Soc.* **1999**, *121* (13), 3214–3217.
- (19) Widmann, D.; Behm, R. J. Activation of Molecular Oxygen and the Nature of the Active Oxygen Species for CO Oxidation on Oxide Supported Au Catalysts. *Acc. Chem. Res.* **2014**, *47* (3), 740–749.
- (20) Bliem, R.; Hoeven, J. Van Der; Zavodny, A.; Gamba, O.; Pavelec, J.; Jongh, P. E. De; Schmid, M.; Diebold, U.; Parkinson, G. S. An Atomic-Scale View of CO and H₂ Oxidation on a Pt/Fe₃O₄ Model Catalyst. *Angew. Chemie* **2015**, *127* (47), 13999–14002.
- (21) Puigdollers, A. R.; Schlexer, P.; Tosoni, S.; Pacchioni, G. Increasing Oxide Reducibility: The Role of Metal/Oxide Interfaces in the Formation of Oxygen Vacancies. *ACS Catal.* **2017**, *7* (10), 6493–6513.
- (22) Zafiris, G. S.; Gorte, R. J. Evidence for Low-Temperature Oxygen Migration from Ceria to Rh. *J. Catal.* **1992**, *139* (2), 561–567.
- (23) Happel, M.; Mysliveček, J.; Johánek, V.; Dvořák, F.; Stetsovych, O.; Lykhach, Y.; Matolín, V.; Libuda, J. Adsorption Sites, Metal-Support Interactions, and Oxygen Spillover Identified by Vibrational Spectroscopy of Adsorbed CO: A Model Study on Pt/Ceria

- Catalysts. *J. Catal.* **2012**, *289*, 118–126.
- (24) Lykhach, Y.; Faisal, F.; Skála, T.; Neitzel, A.; Tsud, N.; Vorokhta, M.; Dvořák, F.; Beranová, K.; Kosto, Y.; Prince, K. C.; Matolín, V.; Libuda, J. Interplay between the Metal-Support Interaction and Stability in Pt/Co₃O₄(111) Model Catalysts. *J. Mater. Chem. A* **2018**, *6* (45), 23078–23086.
- (25) Röttgen, M. A.; Abbet, S.; Judai, K.; Antonietti, J. M.; Wörz, A. S.; Arenz, M.; Henry, C. R.; Heiz, U. Cluster Chemistry: Size-Dependent Reactivity Induced by Reverse Spill-Over. *J. Am. Chem. Soc.* **2007**, *129* (31), 9635–9639.
- (26) Arndt, B.; Lechner, B. A. J.; Bourgund, A.; Grånäs, E.; Creutzburg, M.; Krausert, K.; Hulva, J.; Parkinson, G. S.; Schmid, M.; Vonk, V.; Esch, F.; Stierle, A. Order-Disorder Phase Transition of the Subsurface Cation Vacancy Reconstruction on Fe₃O₄(001). *Phys. Chem. Chem. Phys.* **2020**, *22* (16), 8336–8343.
- (27) Fleet, M. e. The Structure of Magnetite. *Acta Crystallogr. Sect. B Struct. Crystallogr. Cryst. Chem.* **1981**, *37* (4), 917–920.
- (28) Verwey, E. J. W.; Heilmann, E. L. Physical Properties and Cation Arrangement of Oxides with Spinel Structures I. Cation Arrangement in Spinel. *J. Chem. Phys.* **1947**, *15* (4), 174–180.
- (29) Verwey, E. J.; Haayman, P. W.; Romeijn, F. C. Physical Properties and Cation Arrangement of Oxides with Spinel Structures II. Electronic Conductivity. *J. Chem. Phys.* **1947**, *15* (4), 181–187.
- (30) Bliem, R.; McDermott, E.; Ferstl, P.; Setvin, M.; Gamba, O.; Pavelec, J.; Schneider, M. A.;

- Schmid, M.; Diebold, U.; Blaha, P.; Hammer, L.; Parkinson, G. S. Subsurface Cation Vacancy Stabilization of the Magnetite (001) Surface. *Science* **2014**, *346* (6214), 1215–1218.
- (31) Parkinson, G. S. Iron Oxide Surfaces. *Surf. Sci. Rep.* **2016**, *71* (1), 272–365.
- (32) Parkinson, G. S.; Novotny, Z.; Argentero, G.; Schmid, M.; Pavelec, J.; Kosak, R.; Blaha, P.; Diebold, U. Carbon Monoxide-Induced Adatom Sintering in a Pd-Fe₃O₄ Model Catalyst. *Nat. Mater.* **2013**, *12* (8), 724–728.
- (33) Novotny, Z.; Mulakaluri, N.; Edes, Z.; Schmid, M.; Pentcheva, R.; Diebold, U.; Parkinson, G. S. Probing the Surface Phase Diagram of Fe₃O₄(001) towards the Fe-Rich Limit: Evidence for Progressive Reduction of the Surface. *Phys. Rev. B* **2013**, *87* (19), 195410.
- (34) Parkinson, G. S.; Novotný, Z.; Jacobson, P.; Schmid, M.; Diebold, U. A Metastable Fe(A) Termination at the Fe₃O₄(001) Surface. *Surf. Sci.* **2011**, *605* (15–16), L42–L45.
- (35) Hulva, J.; Jakub, Z.; Novotny, Z.; Johansson, N.; Knudsen, J.; Schnadt, J.; Schmid, M.; Diebold, U.; Parkinson, G. S. Adsorption of CO on the Fe₃O₄(001) Surface. *J. Phys. Chem. B* **2018**, *122* (2), 721–729.
- (36) Meier, M.; Hulva, J.; Jakub, Z.; Pavelec, J.; Setvin, M.; Bliem, R.; Schmid, M.; Diebold, U.; Franchini, C.; Parkinson, G. S. Water Agglomerates on Fe₃O₄(001). *Proc. Natl. Acad. Sci.* **2018**, *115* (25), E5642–E5650.
- (37) Pavelec, J.; Hulva, J.; Halwidl, D.; Bliem, R.; Gamba, O.; Jakub, Z.; Brunbauer, F.; Schmid, M.; Diebold, U.; Parkinson, G. S. A Multi-Technique Study of CO₂ Adsorption on Fe₃O₄ Magnetite. *J. Chem. Phys.* **2017**, *146* (1), 01470.

- (38) Heiz, U.; Vanolli, F.; Trento, L.; Schneider, W. D. Chemical Reactivity of Size-Selected Supported Clusters: An Experimental Setup. *Rev. Sci. Instrum.* **1997**, *68* (5), 1986–1994.
- (39) Nečas, D.; Klapetek, P. Gwyddion: An Open-Source Software for SPM Data Analysis. *Cent. Eur. J. Phys.* **2012**, *10* (1), 181–188.
- (40) Bonanni, S.; Ait-Mansour, K.; Hugentobler, M.; Brune, H.; Harbich, W. An Experimental Setup Combining a Highly Sensitive Detector for Reaction Products with a Mass-Selected Cluster Source and a Low-Temperature STM for Advanced Nanocatalysis. *Eur. Phys. J. D* **2011**, *63*, 241–249.
- (41) Kresse, G.; Furthmüller, J. Efficiency of Ab-Initio Total Energy Calculations for Metals and Semiconductors Using a Plane-Wave Basis Set. *Comput. Mater. Sci.* **1996**, *6* (1), 15–50.
- (42) Blöchl, P. E. Projector Augmented-Wave Method. *Phys. Rev. B* **1994**, *50* (24), 953–978.
- (43) Kresse, G.; Joubert, D. From Ultrasoft Pseudopotentials to the Projector Augmented-Wave Method. *Phys. Rev. B - Condens. Matter Mater. Phys.* **1999**, *59* (3), 1758–1775.
- (44) Perdew, J. P.; Burke, K.; Ernzerhof, M. Generalized Gradient Approximation Made Simple. *Phys. Rev. Lett.* **1996**, *77* (18), 3865–3868.
- (45) Anisimov, V. I.; Zaanen, J.; Andersen, O. K. Band Theory and Mott Insulators: Hubbard U Instead of Stoner I. *Phys. Rev. B* **1991**, *44* (3), 943–954.
- (46) Dudarev, S.; Botton, G.; Savrasov, S. Y.; Humphreys, C. J.; Sutton, A. P. Electron-Energy-Loss Spectra and the Structural Stability of Nickel Oxide: An LSDA+U Study. *Phys. Rev. B - Condens. Matter Mater. Phys.* **1998**, *57* (3), 1505–1509.

- (47) Grimme, S.; Antony, J.; Ehrlich, S.; Krieg, H. A Consistent and Accurate Ab Initio Parametrization of Density Functional Dispersion Correction (DFT-D) for the 94 Elements H-Pu. *J. Chem. Phys.* **2010**, *132* (15), 154104.
- (48) Henkelman, G.; Uberuaga, B. P.; Jónsson, H. Climbing Image Nudged Elastic Band Method for Finding Saddle Points and Minimum Energy Paths. *J. Chem. Phys.* **2000**, *113* (22), 9901–9904.
- (49) Zhang, K.; Shaikhutdinov, S.; Freund, H.-J. Does the Surface Structure of Oxide Affect the Strong Metal-Support Interaction with Platinum? Platinum on Fe₃O₄(001) versus Fe₃O₄(111). *ChemCatChem* **2015**, *7* (22), 3725–3730.
- (50) Whitman, L. J.; Richter, L. J.; Gurney, B. A.; Villarrubia, J. S.; Ho, W. Co Adsorption Site Occupations on Fe(111) vs Coverage and Temperature: The Kinetics of Adsorption and Reaction. *J. Chem. Phys.* **1989**, *90* (3), 2050–2062.
- (51) Sun, Y. N.; Qin, Z. H.; Lewandowski, M.; Shaikhutdinov, S.; Freund, H. J. CO Adsorption and Dissociation on Iron Oxide Supported Pt Particles. *Surf. Sci.* **2009**, *603* (20), 3099–3103.
- (52) Parkinson, G. S.; Manz, T. A.; Novotný, Z.; Sprunger, P. T.; Kurtz, R. L.; Schmid, M.; Sholl, D. S.; Diebold, U. Antiphase Domain Boundaries at the Fe₃O₄(001) Surface. *Phys. Rev. B - Condens. Matter Mater. Phys.* **2012**, *85* (19), 1–7.
- (53) Beniya, A.; Higashi, S.; Ohba, N.; Jinnouchi, R.; Hirata, H.; Watanabe, Y. CO Oxidation Activity of Non-Reducible Oxide-Supported Mass-Selected Few-Atom Pt Single-Clusters. *Nat. Commun.* **2020**, *11* (1), 1–10.

- (54) Hulva, J.; Meier, M.; Bliem, R.; Jakub, Z.; Kraushofer, F.; Schmid, M.; Diebold, U.; Franchini, C.; Parkinson, G. S. Unraveling CO Adsorption on Model Single-Atom Catalysts. *Science* **2021**, *371* (6527), 375–379.
- (55) Szabó, A.; Henderson, M. A.; Yates, J. T. Oxidation of CO by Oxygen on a Stepped Platinum Surface: Identification of the Reaction Site. *J. Chem. Phys.* **1992**, *96* (8), 6191–6202.
- (56) Sebetci, A. A Density Functional Study of Bare and Hydrogenated Platinum Clusters. *Chem. Phys.* **2006**, *331* (1), 9–18.
- (57) Xiao, L.; Wang, L. Structures of Platinum Clusters: Planar or Spherical. *J. Phys. Chem. A* **2004**, *108* (41), 8605–8614.
- (58) Yang, S. H.; Drabold, D. A.; Adams, J. B.; Ordejón, P.; Glassford, K. Density Functional Studies of Small Platinum Clusters. *J. Phys. Condens. Matter* **1997**, *9* (5), L39–L45.
- (59) Heredia, C. L.; Ferraresi-Curotto, V.; López, M. B. Characterization of Pt_n (N=2–12) Clusters through Global Reactivity Descriptors and Vibrational Spectroscopy, a Theoretical Study. *Comput. Mater. Sci.* **2012**, *53* (1), 18–24.
- (60) Bhattacharyya, K.; Majumder, C. Growth Pattern and Bonding Trends in Pt_n (n = 2-13) Clusters: Theoretical Investigation Based on First Principle Calculations. *Chem. Phys. Lett.* **2007**, *446* (4–6), 374–379.
- (61) Grönbeck, H.; Andreoni, W. Gold and Platinum Microclusters and Their Anions: Comparison of Structural and Electronic Properties. *Chem. Phys.* **2000**, *262* (1), 1–14.
- (62) Sebetci, A.; Güvenç, Z. B. Energetics and Structures of Small Clusters: Pt_N, N = 2-21. *Surf.*

Sci. **2003**, 525 (1–3), 66–84.

Supporting Information for

Cluster Catalysis with Lattice Oxygen:
Tracing Oxygen Transport from a Magnetite(001)
Support onto Small Pt Clusters

Sebastian Kaiser,^{1,2} Farahnaz Maleki,³ Ke Zhang,^{1,2} Wolfgang Harbich,⁴ Ueli Heiz,^{1,2} Sergio Tosoni,³ Barbara A. J. Lechner,^{1,} Gianfranco Pacchioni,³ Friedrich Esch^{1,2}*

¹ Chair of Physical Chemistry, Department of Chemistry, Technical University of Munich,
Lichtenbergstr. 4, 85748 Garching, Germany

² Catalysis Research Center, Technical University of Munich, Lichtenbergstr. 4, 85748 Garching,
Germany

³ Dipartimento di Scienza dei Materiali, University of Milano-Bicocca, via Roberto Cozzi 55,
20125 Milano, Italy

⁴ Institute of Physics, Ecole Polytechnique Fédérale de Lausanne, CH-1015 Lausanne,
Switzerland

* bajlechner@tum.de

S1. Pulsed reactivity data evaluation

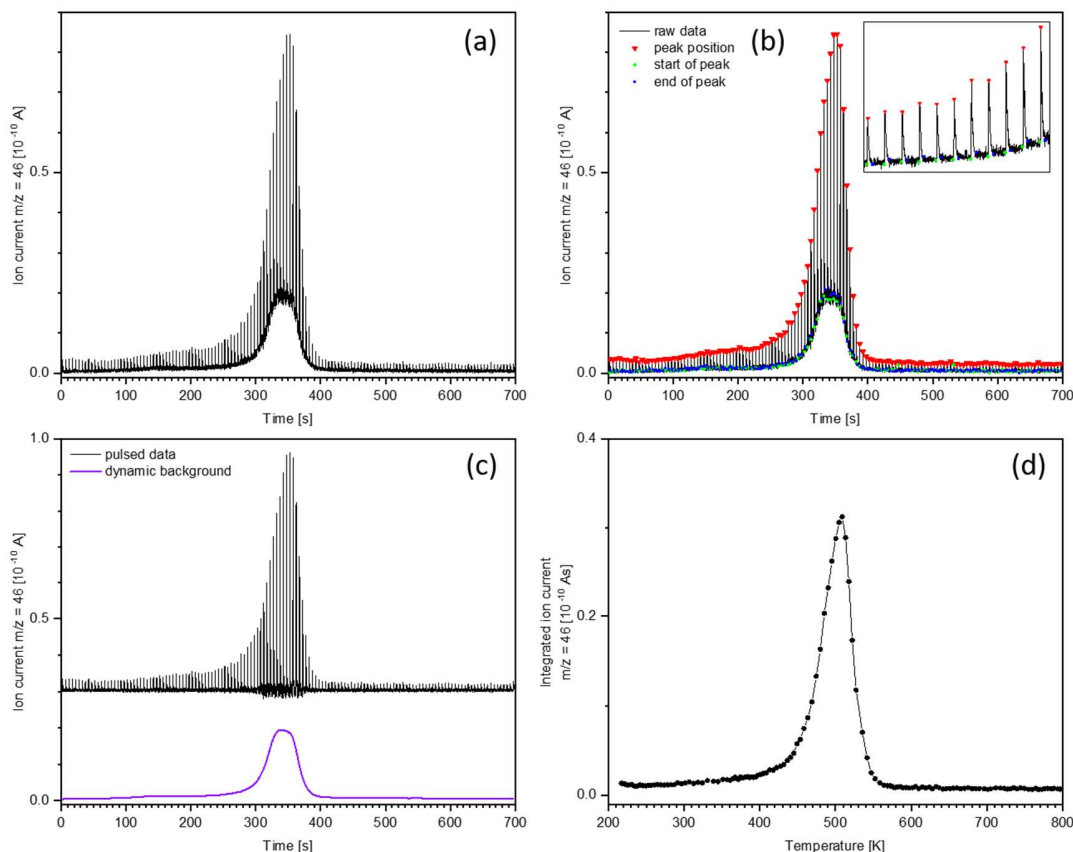


Figure S1. Evaluation procedure for pulsed valve sniffer measurements. (a) displays the measured raw data, consisting of a series of pulses convoluted with a continuous dynamic background (usually caused by desorption or reaction products). As both components contain information about the investigated system, it is necessary to separate them. First, the peak position (red), as well as the start (green) and end (blue) of each peak are detected, as shown in (b). The inset shows a zoomed-in section to better illustrate the method. The data in between the pulses (determined by the start and end points of the pulses) is smoothed and interpolated to determine the dynamic background, which is then subtracted. (c) shows the pulsed data after background subtraction (black, with an offset of 3×10^{-11} A), as well as the subtracted background (purple). Finally, each individual pulse is integrated numerically and the resulting values are plotted vs. temperature, as shown in (d).

S2. Characterization of magnetite bulk and (001) surface by DFT calculations

We started from the experimental crystal structure of Fe_3O_4 using a supercell with a $\text{Fe}_{24}\text{O}_{32}$ ($(\text{Fe}_3\text{O}_4)_8$) formula. Fe_3O_4 (magnetite) has the structure of a cubic inverse spinel with Fe^{3+} in the tetrahedral sites and a 50:50 mixture of Fe^{2+} and Fe^{3+} in the octahedral sites.¹ Tetrahedral and octahedral sublattices are anti-ferrimagnetically aligned in Fe_3O_4 , such that the magnetic moments of the Fe^{3+} cations on each sublattice cancel each other, and a nominal net magnetization of $4 \mu_{\text{B}}$ per Fe_3O_4 formula unit derives from the Fe^{2+} cations. We first optimized the lattice and internal coordinates with PBE+U+D3. The calculated lattice parameters (Table S1) show a slight distortion from the cubic symmetry. The lattice volume is overestimated by 2%, indicating a reasonable agreement of the hereby adopted computational method with the experiment.

Table S1. Calculated and experimental lattice parameters (a, b and c, Å) and cell volume (Å³) of cubic Fe_3O_4 .

| | Calc. | Exp. ^a |
|--------------------|--------|-------------------|
| a | 8.451 | 8.397 |
| b | 8.458 | 8.397 |
| c | 8.458 | 8.397 |
| Cell Volume | 604.59 | 592.1 |

^a Data from ref ²

The calculated electronic structure displays 4 unpaired electrons per formula unit, as reported in experiments (32 unpaired electrons in the unit cell). Figure S2 shows the spin density iso-surface of magnetite. Fe atoms in tetrahedral positions (Fe^{3+}) are spin down while the Fe atoms in octahedral sites are spin up (half Fe^{3+} and half Fe^{2+}), consistent with an anti-ferrimagnetic ordering. In agreement with previous reports adopting a similar level of theory, magnetite is a semimetal, displaying conducting character on one spin channel and a small band gap (≈ 0.5 eV) on the other.

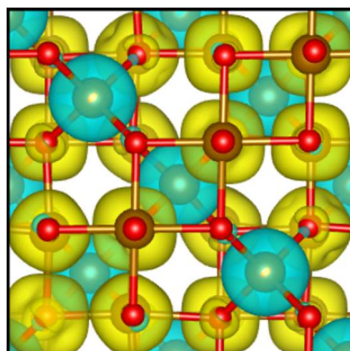


Figure S2. Spin-density iso-surface ($0.01 \text{ |e|/\text{Å}^3}$) of bulk Fe_3O_4 , with α (spin-up) electrons density in yellow and β (spin-down) in cyan.

The magnetite(001) surface is modelled following the sub-surface cation vacancy structure proposed by Parkinson.³ The 1×1 cell's content is $\text{Fe}_{35}\text{O}_{48}$, where one Fe ion in an octahedral site of the subsurface layer has been removed. The hereby adopted slab model contains 12 atomic layers; the ions from the bottom 4 layers are kept frozen in their bulk lattice position, and all others are relaxed. As previously observed,¹ one Fe atom in the second atomic layer moves during the relaxation from an octahedral to a tetrahedral site, Figure S3. There are thus 13 Fe atoms in tetrahedral and 22 Fe atoms in octahedral positions. The total number of unpaired electrons in the supercell is 40 (3.3 per formula unit, showing a remarkable quenching of the magnetic moment with respect to the bulk).

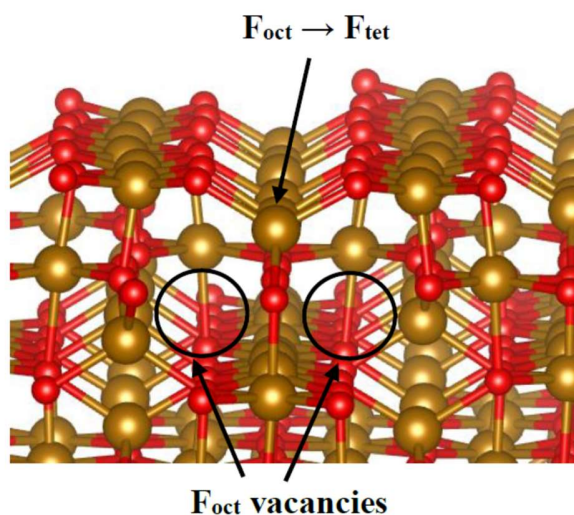


Figure S3. Optimized structure of the subsurface cation vacancy model of $\text{Fe}_3\text{O}_4(001)$.

S3. Formation of a surface oxygen vacancy on various sites

In this section we describe the effect of generating an oxygen vacancy on the surface of magnetite. Given the focus of the present paper on the surface properties of magnetite, we did not consider the vacancy formation in the subsurface and bulk regions. As shown in Figure S4, there are three non-equivalent O atoms on the first atomic layer of the $\text{Fe}_3\text{O}_4(001)$ slab: O1 and O2 are next to an iron atom in a tetrahedral site and O3 is above an iron atom in an octahedral site (Figure S4). The formation energy of an oxygen vacancy (E_f), Table S2, is calculated as follows:

$$E_f = E[\text{Fe}_3\text{O}_{4-x}] + E[\frac{1}{2} \text{O}_2] - E[\text{Fe}_3\text{O}_4] \quad (1)$$

$$E'_f = E[\text{Fe}_3\text{O}_{4-x}] + E[\text{O}] - E[\text{Fe}_3\text{O}_4] \quad (2)$$

The O3 vacancy has the lowest formation energy of 2.91 eV; the other oxygens are removed at a somewhat higher cost, as shown in Table S2. Notably, the formation of a vacancy in O3 increases the net magnetization per formula unit from 3.4 μ_B (pristine surface) to 3.8 μ_B , while the removal of O1 or O2 species has little effect on the magnetization.

Table S2. Formation energy of an oxygen vacancy (E_f computed with respect to $\frac{1}{2} \text{O}_2$ and E'_f computed with respect to atomic O, in eV) and magnetic moment per unit cell (M_{total} , μ_B) on the (001) surface of Fe_3O_4 , illustrated in Figure S4.

| | E_f | E'_f | M_{total} |
|-----------------|-------|--------|--------------------|
| V_{O1} | 3.55 | 6.93 | 3.34 |
| V_{O2} | 3.10 | 6.48 | 3.32 |
| V_{O3} | 2.91 | 6.30 | 3.79 |

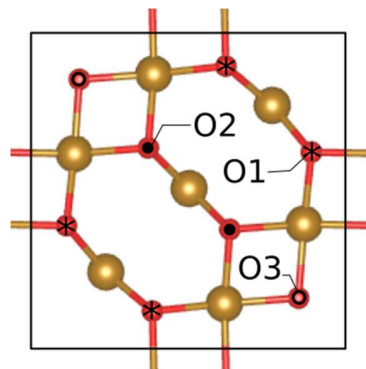


Figure S4. Top view of the first and second atomic layers of the $\text{Fe}_3\text{O}_4(001)$ unit cell. O1, O2 and O3 indicate the non-equivalent O atoms on the surface of the $\text{Fe}_3\text{O}_4(001)$ slab.

S4. CO desorption from bare magnetite and magnetite-supported clusters in TPD

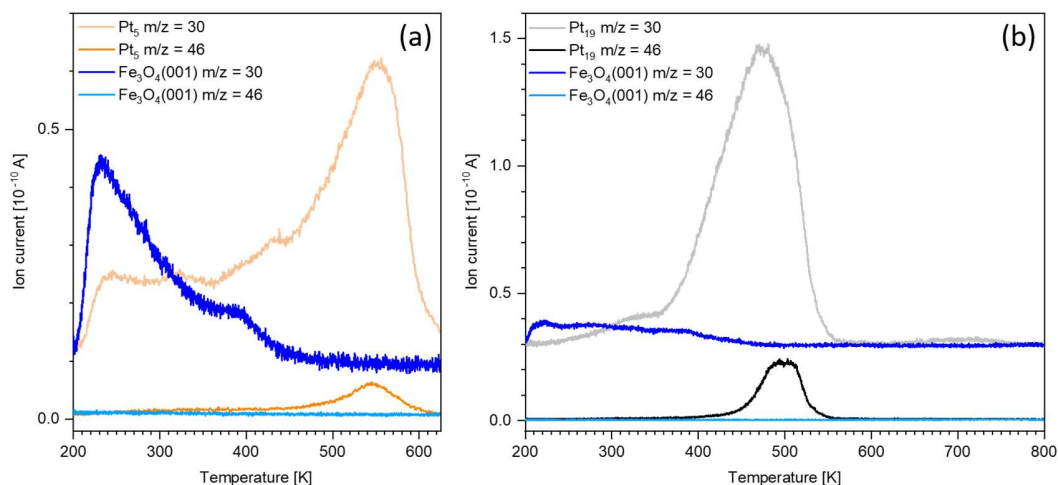


Figure S5. Saturation C¹⁸O TPD curves of (a) Pt₅ (orange) and (b) Pt₁₉ (gray) supported on Fe₃O₄(001) compared to the corresponding desorption curves from the clean support (blue). The heating rate was 1 K/s. The C¹⁸O (m/z = 30) and C¹⁸O¹⁶O (m/z = 46) signals are shown. The clean magnetite surface exhibits several overlapping, not very distinct CO desorption features in the temperature region investigated here. The desorption starts immediately upon heating and is finished below 450 K. These background desorption features are the high temperature shoulder of a much larger desorption peak located around 180 K, which is attributed to an unidentified magnetite surface defect.⁴ It can be observed that especially the beginning of the background CO desorption around 230 K is much less pronounced with clusters deposited on the Fe₃O₄(001) surface, indicating that a part of the defects are no longer accessible CO adsorption sites. This effect can be explained by at least some of the clusters occupying surface defect sites. Furthermore, it is shown that no CO₂ desorption or production from the bare Fe₃O₄(001) surface is detectable in the measured temperature region (cyan).

S5. Ripening of Pt₅ in STM

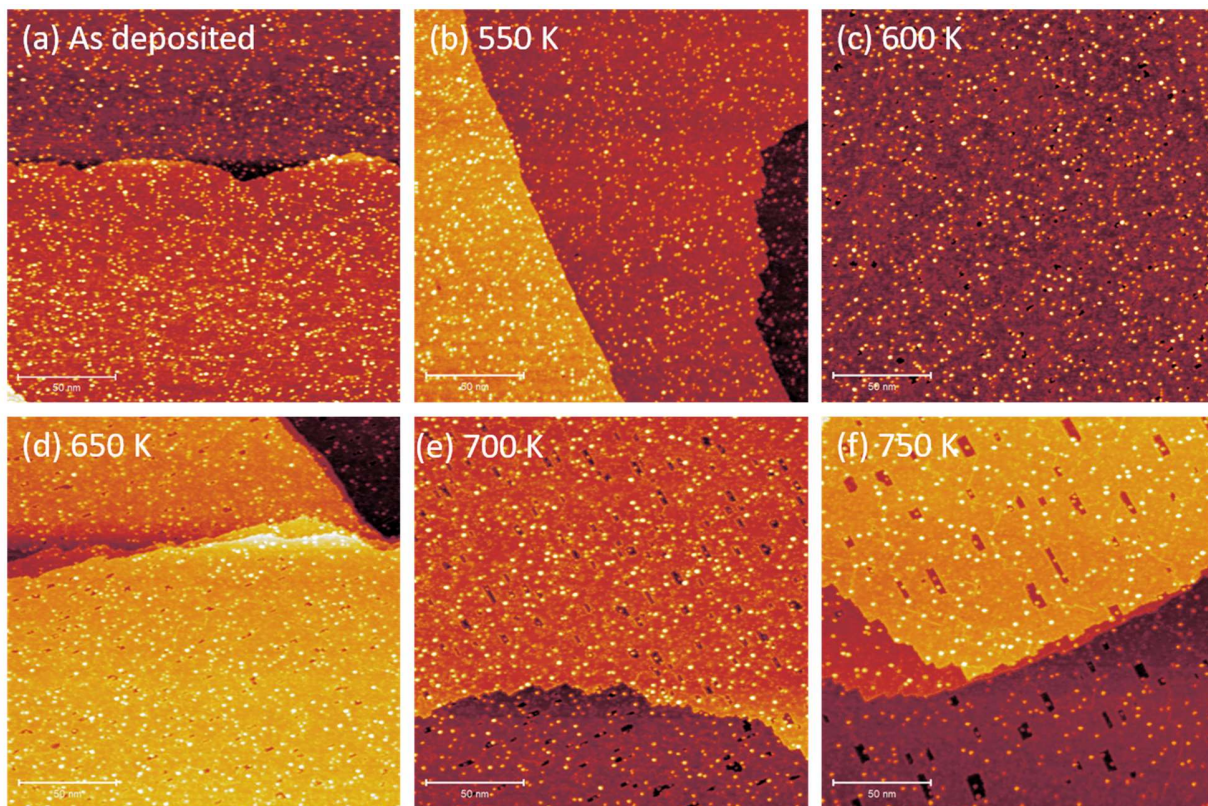


Figure S6. STM image series of Pt₅ clusters (0.05 clusters/nm²) on Fe₃O₄(001), (a) as deposited at RT, (b-f) measured at RT after annealing to the temperatures indicated, respectively. Up to an annealing temperature of 600 K, the number of clusters stays constant. Above 650 K, gradual cluster ripening is observed, yielding fewer clusters with an average size of about Pt₁₅₋₂₀ at 750 K. The approximate size is calculated by comparing the apparent height and number of clusters at 750 K with the as-deposited sample. Upon annealing, hole formation around some clusters is observed, due to lattice oxygen migrating onto the clusters and reaction with background CO, while the residual, reduced iron atoms diffuse into the bulk. *Imaging parameters:* $V_b = 1.50$ V; $I_t = 300$ pA.

S6. Alternating CO and O₂ pulses on Pt₅/Fe₃O₄(001)

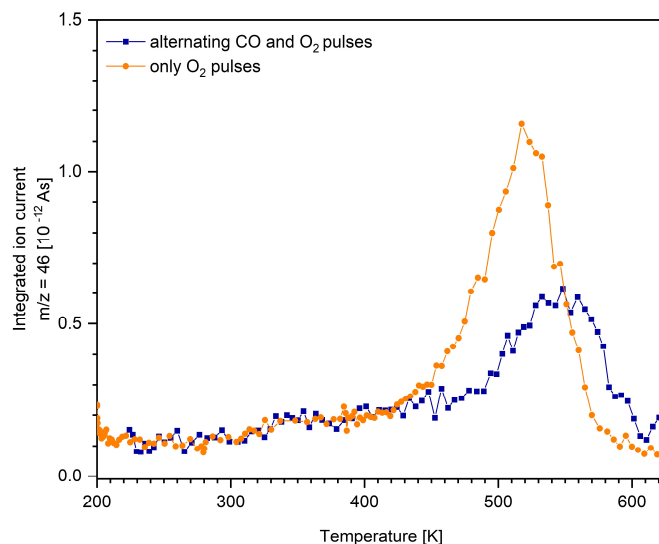


Figure S7. CO₂ production synchronized with O₂ pulses as a function of temperature, obtained by pulsing only O₂ (orange) and alternately pulsing CO and O₂ (blue) on CO pre-covered Pt₅ clusters on Fe₃O₄(001). Both curves have been normalized to the Pt atom coverage. When additionally pulsing CO, the onset of the CO₂ production peak synchronized with O₂ pulses is shifted to higher temperatures, indicating a stronger initial poisoning of the cluster surface by CO since the CO pulses shift the desorption equilibrium. The peak position is similarly shifted from 520 K to 550 K. This indicates a reaction limitation due to a lack of CO when only pulsing O₂.

S7. Loss of CO adsorption capability upon cluster encapsulation

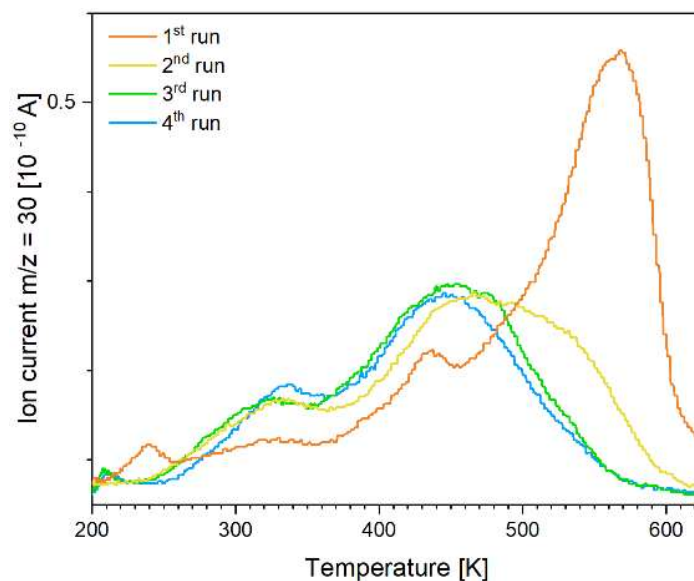


Figure S8. Subsequent saturation C^{18}O TPD curves ($m/z = 30$) of Pt_5 clusters (0.05 clusters/ nm^2) on $\text{Fe}_3\text{O}_4(001)$, corresponding to the TPD experiments shown in Figure 2. For every run, the surface was saturated with C^{18}O at 200 K, the heating rate was 1 K/s. The main peak in the first run (orange) at 550 K is attributed to the clusters. Several lower temperature features are observed as well, which most certainly are related to surface defects (as described in section 3.1 in the main text). In the second run (yellow) the cluster-related desorption feature decreases significantly, while two broad lower temperature peaks arise at 325 K and 450 K. In the third TPD run (green), the CO desorption from the cluster vanishes almost completely, while the lower temperature peaks become slightly more pronounced. In the fourth run (blue), only the lower temperature peaks occur. This subsequent decrease in CO adsorption capability of the clusters is attributed to encapsulation as a result of SMSI, comparable to Pt nanoparticles supported on $\text{Fe}_3\text{O}_4(001)$ that become encapsulated by an FeO layer upon annealing.⁵ The TPD series indicates that after the first run, the clusters are partially encapsulated, with still a fraction of their surface accessible for CO adsorption. In the following runs, the clusters become completely encapsulated, thus no cluster-related CO desorption is observed anymore. The lower temperature features appear simultaneously with the encapsulation of the clusters and may therefore originate from CO desorption from the encapsulating layer, which is expected to be non-stoichiometric, reduced iron oxide, since the lower temperature peaks are well within the temperature range of CO desorption from FeO surfaces.⁶ However, more experiments have to be done for further clarification.

S8. Hole formation in cluster vicinity

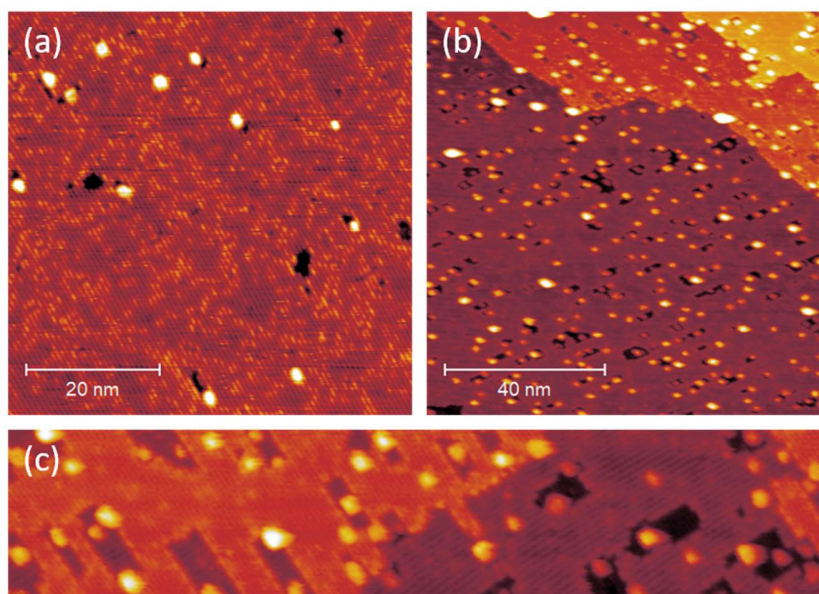


Figure S9. Hole formation around Pt clusters on Fe₃O₄(001). (a) shows Pt₁₀ clusters (0.01 clusters/nm²) measured at 573 K. Clear hole formation around the cluster perimeter can be observed caused by the removal of lattice oxygen around the clusters by reverse spillover and reaction with CO from the chamber background, followed by Fe migration into the bulk. (b) and (c) display Pt₁₉ (0.05 clusters/nm²) measured at RT after annealing to 590 K in 1×10^{-7} mbar CO for 2 minutes. Again, hole formation around the clusters can be observed, but much more pronounced compared to samples annealed in UHV as a consequence of the higher CO partial pressure. The holes exhibit a rectangular shape which changes direction between two neighboring terraces, following the direction of the atomic rows of the support. This becomes very obvious in the zoomed-in area in (c). The holes are fairly large compared to the clusters, indicating a facile oxygen diffusion towards the clusters at elevated temperatures. The edges of the holes are straight and terminated by an iron row of the magnetite lattice, but more rough perpendicular to them. This indicates that the oxygen diffusion is more favorable along an atomic row, suggesting the initial removal of an oxygen atom from a pristine atomic row to be most difficult. *Imaging parameters:* $V_b = 1.50$ V; (a) $I_t = 500$ pA, (b, c) $I_t = 300$ pA.

S9. Platinum clusters in the gas phase: structure relaxation and oxygen adsorption

The minimum energy structures of gas phase Pt clusters have been studied in previous DFT investigations.⁷⁻¹³ For instance, the calculations with a B3PW91 hybrid functional show that a Pt₅ cluster with distorted squared pyramid geometry, Figure S10(iii), is the lowest energy isomer.⁷ Here, we have considered six of the most stable isomers, and recomputed their stabilities and structures at the PBE+U+D3 level, Figure S10. Four isomers are within an energy of 200 meV, and all six isomers are within 0.35 eV, with energy differences of 70-80 meV, respectively. This suggests a high fluxionality in the gas phase. Of course, once deposited on an oxide support, the structural flexibility of the Pt clusters could be reduced.

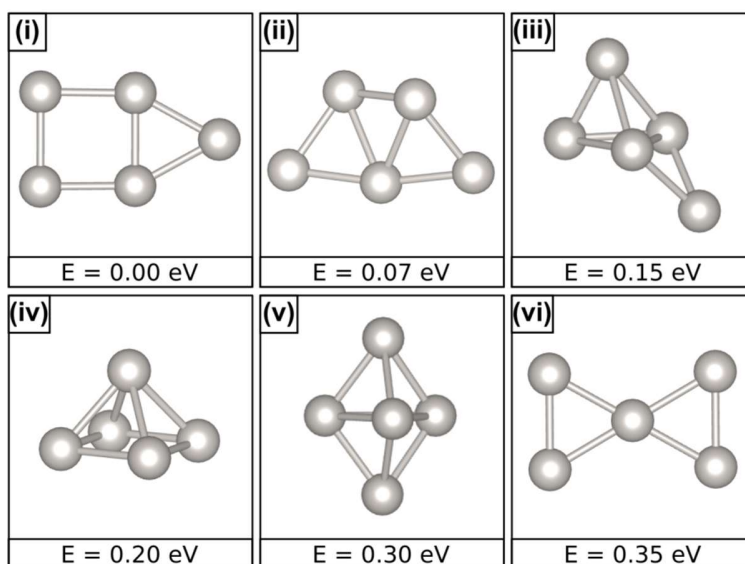


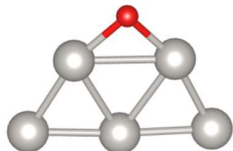
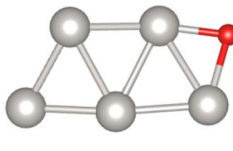
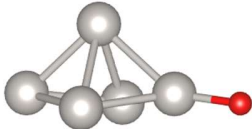
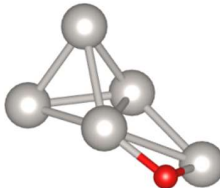
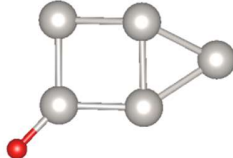
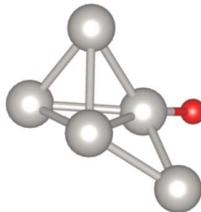
Figure S10. Optimized structures and relative energies of isomers of the Pt₅ gas phase cluster.

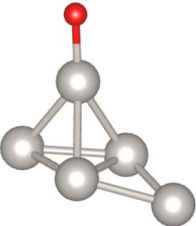
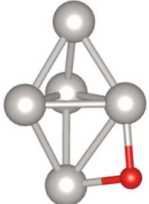
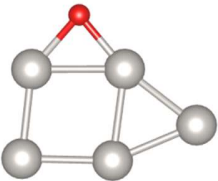
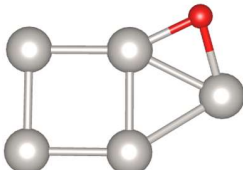
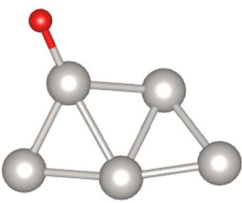
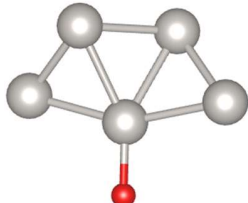
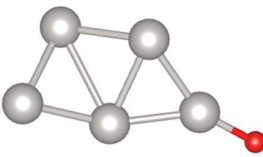
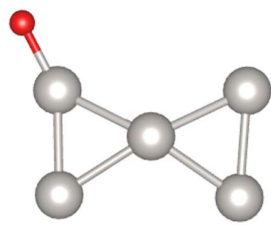
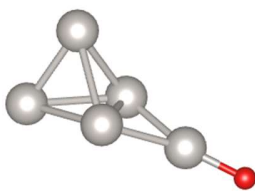
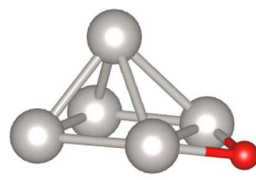
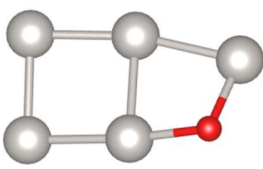
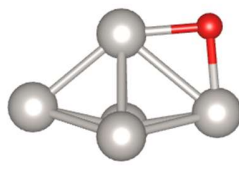
We consider the preferred adsorption sites for a single O atom on the various isomers of gas phase Pt₅. Altogether, we have considered 25 possible structures, and this is not necessarily an exhaustive sample. The adsorption of an O atom on the (i) to (vi) Pt₅ clusters, summarized in Table S3, occurs in three positions: terminal, bridge and hollow. In many cases, the position of the adsorbed O atom and/or the shape of cluster change during optimization. Table S3 reports the optimized structures, their relative energy (E_R), and the adsorption energy (E_{ADS}) of an O atom with respect to the most stable Pt₅ (i) cluster and $\frac{1}{2}$ O₂ molecule, calculated as follows:

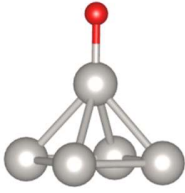
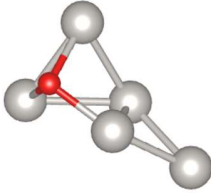
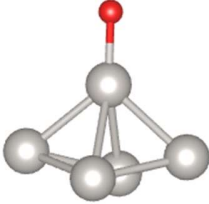
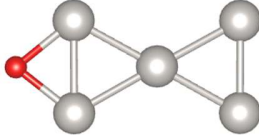
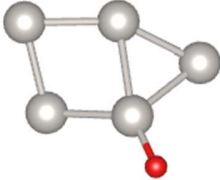
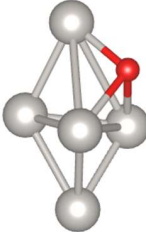
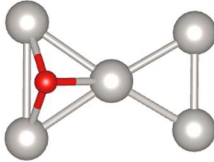


The most stable gas phase Pt₅O cluster is planar, with the Pt atoms forming three fused triangles and the O atom adsorbed in a Pt-Pt bridge position. The next most stable isomer has a completely different structure: it is three-dimensional with the adsorbed O in a terminal position, bound to an apical Pt atom. It is 0.42 eV higher in energy than the ground state structure. Also the next two stable isomers 3 and 4, Table S3, show the presence of O in a terminal position. In general, an O atom binds preferentially in a Pt-Pt bridge site only if the Pt-Pt distance is such to favour its coordination. Cases where the O atom is in a hollow site are clearly higher in energy.

Table S3. Relative energy (E_R) and adsorption energy (E_{ADS}) of an adsorbed O atom on Pt₅ clusters.

| Structure | E_R , eV | E_{ADS} , eV | Structure | E_R , eV | E_{ADS} , eV |
|--|------------|----------------|--|------------|----------------|
| 1  | 0.00 | -2.42 | 13  | 0.95 | -1.47 |
| 2  | 0.42 | -2.00 | 14  | 0.98 | -1.44 |
| 3  | 0.53 | -1.89 | 15  | 1.09 | -1.33 |

| | | | | | | | |
|---|---|------|-------|----|--|------|-------|
| 4 |  | 0.63 | -1.80 | 16 |  | 1.11 | -1.31 |
| 5 |  | 0.65 | -1.78 | 17 |  | 1.16 | -1.27 |
| 6 |  | 0.67 | -1.75 | 18 |  | 1.18 | -1.24 |
| 7 |  | 0.67 | -1.75 | 19 |  | 1.21 | -1.21 |
| 8 |  | 0.77 | -1.65 | 20 |  | 1.26 | -1.17 |
| 9 |  | 0.83 | -1.60 | 21 |  | 1.30 | -1.12 |

| | | | | | | | |
|----|--|------|-------|----|--|------|-------|
| 10 |  | 0.83 | -1.59 | 22 |  | 2.11 | -0.31 |
| 11 |  | 0.86 | -1.56 | 23 |  | 2.12 | -0.30 |
| 12 |  | 0.91 | -1.52 | 24 |  | 2.18 | -0.24 |
| | | | | 25 |  | 2.22 | -0.20 |

S10. Adsorption of Pt₅ on Fe₃O₄(001) and formation of oxygen vacancies

Table S4. Adsorption energy (E_{ADS} , eV), Bader charge (q , |e|), and spin polarization of adsorbed Pt₅ clusters on Fe₃O₄ and total spin magnetic moment per unit cell (M_{total} , μ_{B}).

| Figure | $E_{\text{ADS}}^{(a)}$ | $q(\text{Pt}_5)$ | $M(\text{Pt}_5)$ | M_{total} |
|--------|------------------------|------------------|------------------|--------------------|
| 4(a) | -4.51 | 0.33 | 0.08 | 2.59 |
| 4(b) | -3.01 | 0.25 | 1.12 | 3.17 |
| 4(c) | -2.73 | 0.33 | 0.19 | 3.22 |

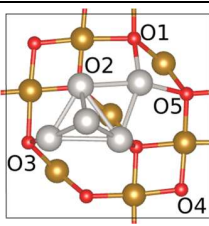
^(a) Energy change related to the reaction $\text{Pt}_5(\text{i}) + \text{Fe}_3\text{O}_4 \rightarrow \text{Pt}_5(\text{n})/\text{Fe}_3\text{O}_4$

The Pt₅ adsorption energies, reported in Table S4, are calculated with respect to the clean support and the gas phase cluster in its most stable configuration (capped square, Figure S10(i)).

The formation energy of the oxygen vacancy (E_f), Table S5, has been calculated according to the following equation:

$$E_f = E[(\text{Pt}_5/\text{Fe}_3\text{O}_{4-x})] + E[\frac{1}{2} \text{O}_2] - E[(\text{Pt}_5/\text{Fe}_3\text{O}_4)] \quad (4)$$

Table S5. O vacancy energy (E_f , eV), Bader charge (q , |e|), spin polarization of an adsorbed Pt₅ cluster (Figure 4(a)) and total spin magnetic moment per unit cell (M , μ_{B}). The position of the O atom removed is shown in the Figure.

| | E_f | $q(\text{Pt}_5)$ | $M(\text{Pt}_5)$ | M_{total} | |
|-----------------|-------|------------------|------------------|--------------------|--|
| V _{O1} | 3.14 | -0.27 | 0.20 | 2.61 |  |
| V _{O2} | 1.98 | -0.37 | 0.27 | 3.24 | |
| V _{O3} | 2.66 | -0.50 | 0.28 | 2.49 | |
| V _{O4} | 2.46 | 0.24 | 0.35 | 3.40 | |

As discussed in the main text, we observe a general decrease in the formation energy in the presence of the platinum clusters with respect to the clean support. The reduction of the substrate upon oxygen removal, however, does not imply a remarkable charge transfer to the cluster, as shown by the Bader charges. In some cases, in particular V_{O1} and V_{O3}, a significant decrease of the net magnetization is reported.

S11. Lattice oxygen reverse spillover

(i) Displacement of one oxygen atom

The study of the formation of an O vacancy on the clean support has shown that O₂ is the easiest O to remove, as shown in Table S5. In this section, we consider the energetic cost of displacing the O₂ atom from the support and adsorbing it on a Pt₅ cluster. The process corresponds to the final state of a lattice oxygen reverse spillover effect. The O atom has been re-adsorbed on various sites of the supported Pt₅ cluster, always starting from the most stable structure, Figure 4(a) in the main text, corresponding to the Pt₅(iii) gas phase isomer. Other structures have also been considered, some of them being unstable. For instance, O adsorption on one of the triangular facets of Pt₅ always resulted in an O atom bound to a bridge site. The most stable isomers found are shown in Figure S11 in order of stability (see also Table S6).

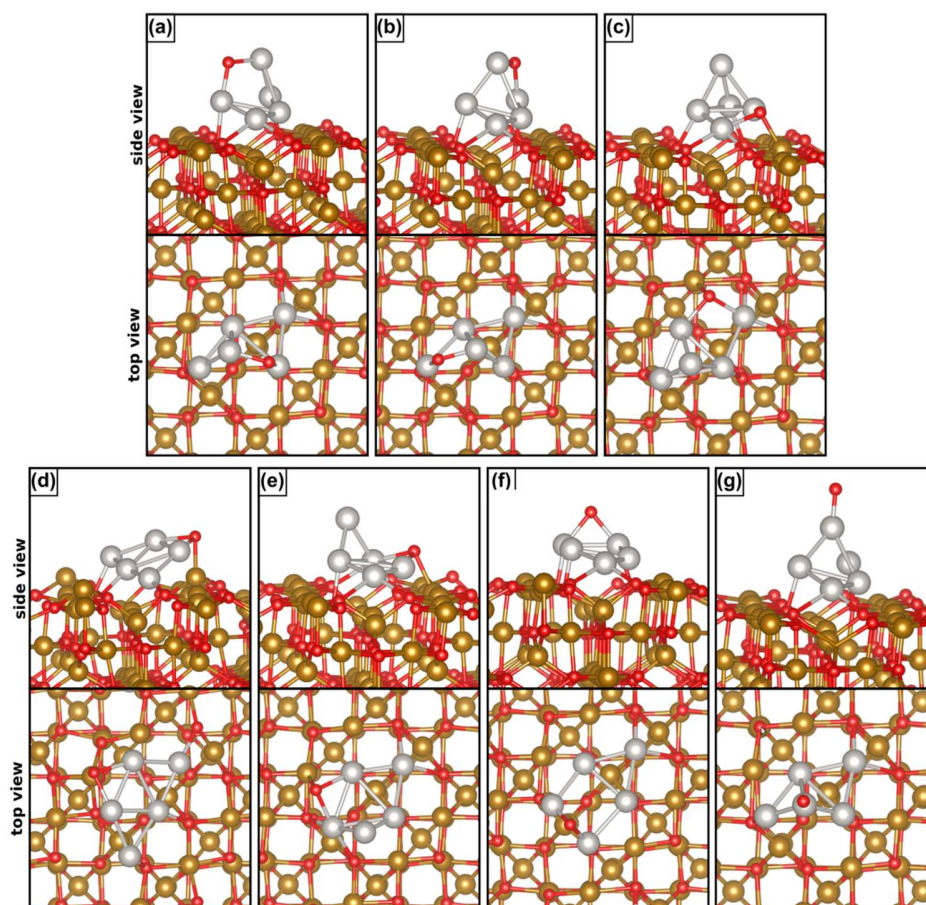


Figure S11. Various isomers of Pt₅O supported on Fe₃O₄. The structures have been obtained starting the geometry optimization from Pt₅/Fe₃O₄, Figure 4(a).

The most stable structure is that of a capped rhombus Pt₅ with an O atom adsorbed on one bridge site, shown in Figure S11(a). The corresponding energy is -0.40 eV lower than that of Pt₅/Fe₃O₅ (see Table S6).

Table S6. O reverse spillover energy (E_{SO} , eV), Bader charge (q , |e|), spin polarization of Pt₅/Fe₃O₄(001) and the total spin magnetic moment per unit cell (M_{total} , μ_{B}).

| Figure | $E_{\text{SO}}^{(a)}$ | $q(\text{Pt}_5)$ | $q(\text{O}_{\text{spill}})$ | $M(\text{Pt}_5)$ | M_{total} |
|---------|-----------------------|------------------|------------------------------|------------------|--------------------|
| S10 (a) | -0.40 | 0.25 | -0.68 | 0.03 | 3.26 |
| S10 (b) | -0.15 | 0.29 | -0.68 | 0.70 | 3.32 |
| S10 (c) | -0.04 | 0.67 | -0.86 | 0.48 | 3.27 |
| S10 (d) | 0.40 | 0.14 | -0.82 | 0.98 | 3.80 |
| S10 (e) | 0.74 | 0.27 | -0.81 | 0.08 | 4.51 |
| S10 (f) | 0.86 | 0.40 | -0.72 | 0.07 | 3.92 |
| S10 (g) | 1.68 | 0.22 | -0.57 | 0.13 | 3.46 |

^(a) E_{SO} refers to the energy of this reaction: $\text{Pt}_5/\text{Fe}_3\text{O}_4 \rightarrow \text{O-Pt}_5/\text{Fe}_3\text{O}_{4-x}$

This shows that the lattice oxygen reverse spillover in this specific case is an exothermic process. A second isomer, Figure S11(b), is only 0.25 eV higher in energy and differs from the isomer of Figure S11(a) only for the Pt-Pt bond that is bridge-bonded by O. A third interesting structure is shown in Figure S11(c). Here, the O atom is bridging a Pt-Pt bond at the cluster/oxide interface. It can be considered the first step in the migration of an O atom from the support onto the cluster. The isomer shown in Figure S11(c) is -0.04 eV lower in energy than the starting structure, i.e. is thermoneutral with respect to the case where no O vacancy has been formed on the support, and no oxygen has been transferred to Pt₅. Other Pt₅O isomers are shown in Figure S11(d)-(g); they are all higher in energy than the three best structures shown in Figure S11(a)-(c).

(ii) *Displacement of two oxygen atoms*

Next, we have considered the spillover of two oxygen atoms from the magnetite surface onto Pt₅. Different O atoms have been removed from the support, and different adsorption positions have been considered on Pt₅O, starting from the most stable structures obtained for the case of a single O reverse spillover, as shown Figure S11. The results are reported in Figure S12 and Table S7.

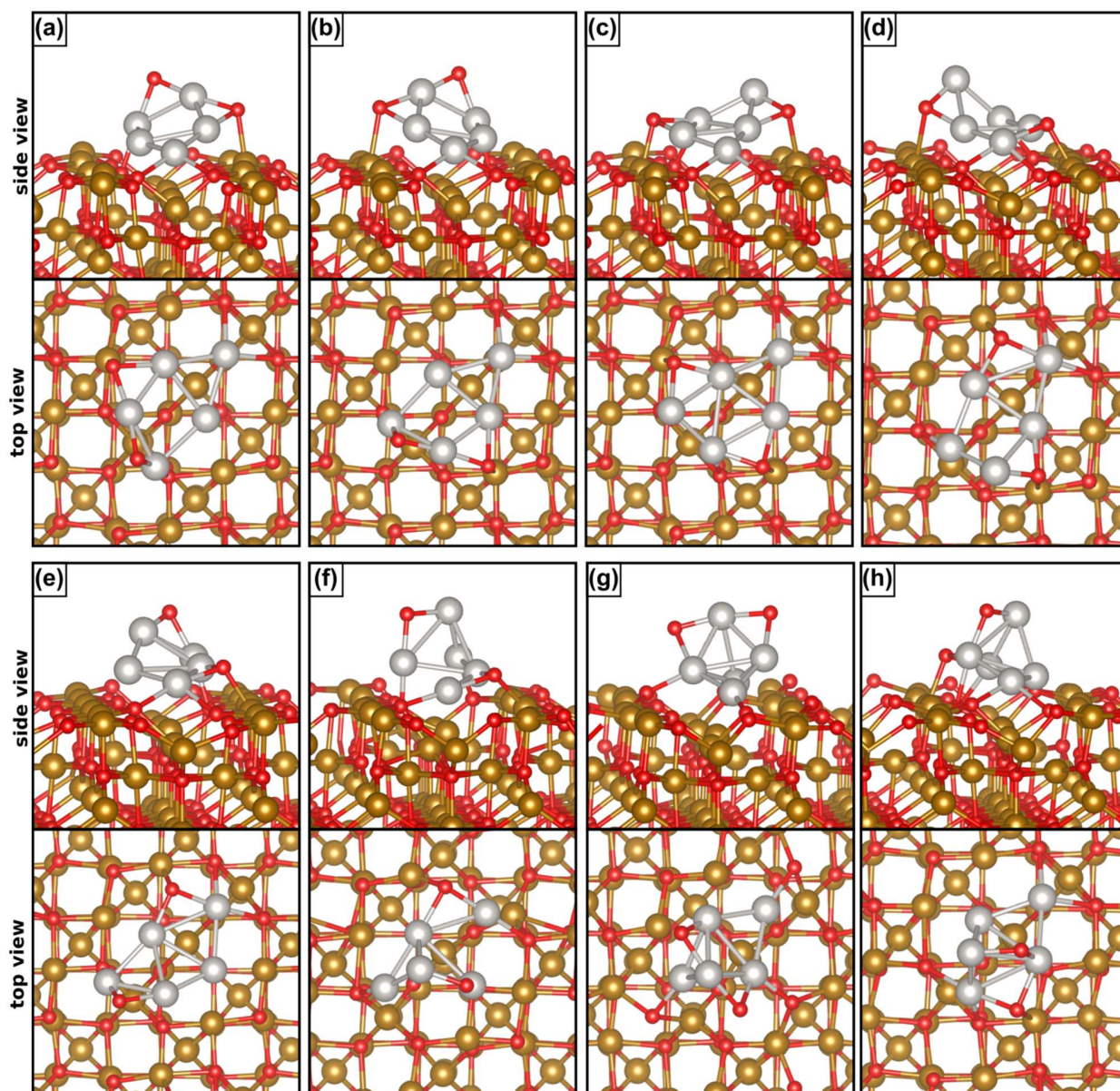


Figure S12. Various isomers of Pt_5O_2 supported on $\text{Fe}_3\text{O}_{4-x}$. The structures have been obtained starting the geometry optimization from $\text{Pt}_5\text{O}/\text{Fe}_3\text{O}_{4-x}$, Figure 5(a). (a) to (d) O2 and O4 spillover; (e) O1 and O2 spillover; (g) and (h) O2 and O4 spillover (see Table S5).

We found two isomers, shown in Figure S12(a) and (b) whose structures are *lower* in energy, by -0.64 and by -0.56 eV, Table S7, than the regular, non-defective surface with adsorbed Pt_5 . This is an important result which shows that multiple oxygen transfer from the support to a small Pt cluster is thermodynamically favorable, and by a considerable amount. These two structures have been obtained by removing the O2 and O4 atoms of the surface, just under the Pt_5 cluster, as shown in

Figure 5(b) in the main text. An important observation is that after geometry optimization, the Pt₅O₂ cluster changes its structure and from 3D (Figure S11(a)) it becomes nearly flat, as shown in Figure S12(a) and (b).

Pt₅ structures that maintain the original 3D shape, a capped rhombus (Figures S10(f) and (g)), are slightly below or slightly above the Pt₅/Fe₃O₄ reference, but clearly higher in energy than the nearly 2D ground state structures.

These results show two important trends: (1) multiple lattice oxygen reverse spillover is an energetically favorable process; and (2) the adsorption of two oxygen atoms on Pt₅ leads to a restructuring that tends to flatten the cluster structure. In order to confirm these trends, in the next Section we considered the spillover of three oxygen atoms.

Table S7. Oxygen spillover energy (E_{SO} , eV), Bader charge (q , |e|), spin polarization of Pt₅/Fe₃O₄(001) and the total spin magnetic moment per unit cell (M , μ_B).

| | Figure | $E_{SO}^{(a)}$ | $q(\text{Pt}_5)$ | $q(2\text{O}_{\text{spill}})$ | $M(\text{Pt}_5)$ | M_{total} |
|--------|---------|----------------|------------------|-------------------------------|------------------|--------------------|
| O2, O4 | S11 (a) | -0.64 | 0.37 | -1.52 | 0.21 | 2.54 |
| | S11 (b) | -0.56 | 0.48 | -1.50 | 0.15 | 3.92 |
| | S11 (c) | 0.59 | 0.41 | -1.62 | 0.19 | 3.96 |
| | S11 (d) | 0.83 | 0.46 | -1.61 | 0.19 | 3.93 |
| | S11 (e) | 0.86 | 0.49 | -1.52 | 0.56 | 2.54 |
| O1, O2 | S11 (f) | 0.30 | 0.53 | -1.58 | 0.65 | 3.34 |
| O2, O4 | S11 (g) | -0.04 | 0.73 | -1.40 | 0.35 | 3.18 |
| | S11 (h) | 1.66 | 1.07 | -1.46 | 0.40 | 3.99 |

^(a) E_{SO} refers to the process: Pt₅/Fe₃O₄ → 2O-Pt₅/Fe₃O_{4-x}

(iii) *Displacement of three oxygen atoms*

We finally considered the case where three oxygens are displaced from the magnetite surface onto the Pt₅ cluster, with formation of a Pt₅O₃ unit and three oxygen vacancies. The number of potential isomers is huge, and we restricted the analysis to the sites where oxygen is easier to remove, O1, O2, and O4 or O1, O2 and O5, and to a few structures derived from the best isomers of Pt₅O₂, as shown in Figure S13 and Table S8. The two most stable structures are shown in Figure S13 (a) and (b) and correspond to a flat or nearly flat Pt₅ with three oxygen atoms in bridge sites; some of them remain coordinated to Fe atoms of the support, thus providing anchoring points for the nanocluster. These two structures are only 0.17 and 0.23 eV higher in energy, respectively, than the pristine Pt₅/Fe₃O₄, showing that even the transfer of three oxygen atoms is energetically

possible (the reaction is only slightly endothermic). We cannot exclude that some more favorable isomers exist, but this already provides sufficient evidence that multiple oxygen transfer from magnetite to supported Pt clusters is possible.

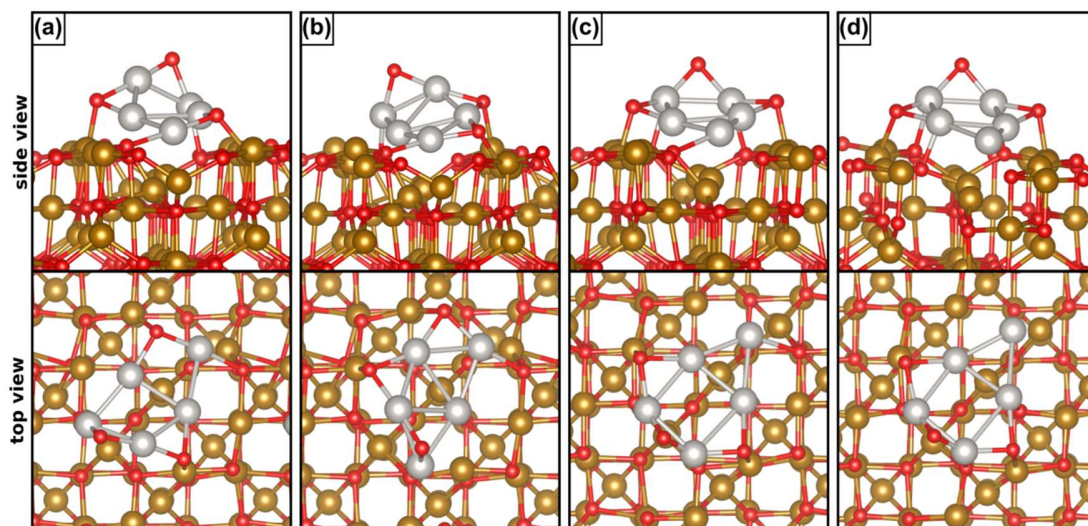


Figure S13. Various isomers of Pt_5O_3 supported on $\text{Fe}_3\text{O}_{4-x}$. The structures have been obtained starting the geometry optimization from $\text{Pt}_5\text{O}_2/\text{Fe}_3\text{O}_{4-x}$, (a) to (c) O1, O2 and O4 spillover; (d) O1, O2 and O5 spillover (see Table S5).

Table S8. Three O spillover energy (E_{SO} , eV), Bader charge (q , |e|), spin polarization of $\text{Pt}_5/\text{Fe}_3\text{O}_4(001)$ and the total spin magnetic moment per unit cell (M , μ_{B}).

| Figure | $E_{\text{SO}}^{(a)}$ | $q(\text{Pt}_5)$ | $q(3\text{O}_{\text{spill}})$ | $M(\text{Pt}_5)$ | M_{total} |
|---------|-----------------------|------------------|-------------------------------|------------------|--------------------|
| S12 (a) | 0.17 | 0.85 | -2.43 | 0.31 | 3.16 |
| S12 (b) | 0.23 | 1.00 | -2.48 | 0.10 | 4.58 |
| S12 (c) | 0.95 | 0.71 | -2.35 | 0.79 | 2.57 |
| S12 (d) | 3.85 | 0.93 | -2.68 | 0.11 | 3.33 |

^(a) E_{SO} refers to the process: $\text{Pt}_5/\text{Fe}_3\text{O}_4 \rightarrow 3\text{O-Pt}_5/\text{Fe}_3\text{O}_{4-x}$

S12. Impact of lattice oxygen reverse spillover on cluster height

In Table S9 we provide some evidence that the lattice oxygen reverse spillover mechanism, with formation of Pt_xO_y clusters, can contribute to a structural change and in particular to a transition from 3D to 2D. For all the structures considered, we have computed the average vertical distance of the Pt atoms from the surface of magnetite. Since the atoms of the surface may be involved in structural changes, we have taken the vertical distance of the Pt atoms from the bottom layer of our slab, whose coordinates are fixed. The most stable Pt_5 cluster, shown in Figure 4 (a) in the main text, is taken as reference. We define ΔZ as the difference of the average distance of the Pt atoms in the various oxidized clusters (see Figures S10 and S11).

The most stable Pt_5O cluster (see Figure S11 (a)), exhibits $\Delta Z = -0.102 \text{ \AA}$; the most stable Pt_5O_2 cluster (see Figure S12 (a)) has $\Delta Z = -0.386 \text{ \AA}$; and the most stable Pt_5O_3 cluster (see Figure S13 (a)) has $\Delta Z = -0.426 \text{ \AA}$. This trend is not fortuitous and is found also for the other most stable Pt_xO_y clusters, as shown in Table S9. The physical reason for this is that some of the O atoms bind at the cluster periphery, and interact also with Fe ions on the surface. In order to increase this bonding, the cluster flattens its structure, resulting in a transition from 3D to 2D.

Table S9. Different distances of Pt_5O_x clusters to the magnetite support with respect to $\text{Pt}_5/\text{Fe}_3\text{O}_4$.

| | Figures | $Z_{\text{avg}}(\text{\AA})$ | $\Delta Z(\text{\AA})$ |
|-------------------------------------|--------------|------------------------------|------------------------|
| $\text{Pt}_5/\text{Fe}_3\text{O}_4$ | 4 (a) | 13.734 | 0.000 |
| | 4 (b) | 13.908 | 0.174 |
| | 4 (c) | 13.424 | -0.310 |
| One O spillover | S10 (a) | 13.632 | -0.102 |
| | S10 (b) | 13.662 | -0.072 |
| | S10 (c) | 13.735 | 0.001 |
| | S10 (d) | 13.478 | -0.256 |
| | S10 (e) | 13.419 | -0.315 |
| | S10 (f) | 13.245 | -0.489 |
| | S10 (g) | 13.631 | -0.103 |
| Two O spillover | S11 (a) | 13.348 | -0.386 |
| | S11 (b) | 13.344 | -0.390 |
| | S11 (c) | 13.408 | -0.326 |

| | | | |
|--|---------|--------|--------|
| | S11 (d) | 13.414 | -0.320 |
| | S11 (e) | 13.284 | -0.450 |
| | S11 (f) | 13.547 | -0.187 |
| | S11 (g) | 13.512 | -0.222 |
| | S11 (h) | 13.478 | -0.256 |
| Three O spillover | S12 (a) | 13.308 | -0.426 |
| | S12 (b) | 13.435 | -0.299 |
| | S12 (c) | 13.172 | -0.562 |
| | S12 (d) | 13.312 | -0.062 |
| $Z_{\text{avg}} = \Sigma z(\text{Fe},\text{O}) \text{ bottom layer}/m - \Sigma z(\text{Pt}) \text{ cluster}/n$ $\Delta Z = Z_{\text{avg}}(\text{Pt}_x\text{O}_y) - Z_{\text{avg}}(\text{Pt}_5)$ | | | |

S13. Iron spillover

There are two kinds of non-equivalent Fe atoms on the first and second atomic layers of the $\text{Fe}_3\text{O}_4(001)$ slab: Fe atoms in the octahedral and tetrahedral positions, respectively, as shown in Figure S14. The formation energy of an Fe vacancy (E_f), listed in Table S10, is calculated according to the following equations:

$$E_f = E[\text{Fe}_{3-x}\text{O}_4] + E[\text{Fe}(\text{s})] - E[\text{Fe}_3\text{O}_4] \quad (5)$$

$$E'_f = E[\text{Fe}_{3-x}\text{O}_4] + E[\text{Fe}(\text{g})] - E[\text{Fe}_3\text{O}_4] \quad (6)$$

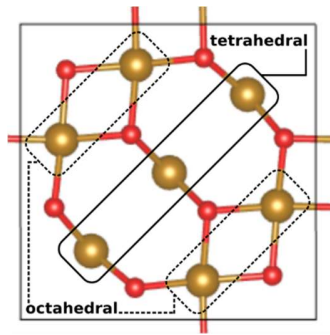


Figure S14. Top view of the first and second atomic layers of the $\text{Fe}_3\text{O}_4(001)$ unit cell. Fe atoms in octahedral and tetrahedral sites on the surface of an $\text{Fe}_3\text{O}_4(001)$ slab are marked by dashed and full lines, respectively.

Table S10. Formation energy of an iron vacancy (E_f computed with respect to solid Fe and E'_f , computed with respect to atomic Fe, in eV) and magnetic moment per unit cell (M_{total} , μ_B) on the (001) surface of Fe_3O_4 .

| | E_f | E'_f | M_{total} |
|--|-------|--------|--------------------|
| $\text{Fe}_{3-x}\text{O}_4$ ($V_{\text{Fe_tetrahedral}}$) | 6.60 | 9.35 | 3.69 |
| $\text{Fe}_{3-x}\text{O}_4$ ($V_{\text{Fe_octahedral}}$) | 6.64 | 9.39 | 2.08 |

Here, we discuss the Fe vacancy formation for the case of the most stable $\text{Pt}_5/\text{Fe}_3\text{O}_4$ structure (Figure 4(a)). As shown in Figure S15, there are 7 non-equivalent Fe atoms in the first and second atomic layers of the $\text{Fe}_3\text{O}_4(001)$ slab. We have considered two vacancies in tetrahedral (F1 and F2 shown in Figure S15) and two vacancies in octahedral (F3 and F4 shown in Figure S15) positions on the surface of the $\text{Pt}_5/\text{Fe}_3\text{O}_4$ structure. The optimized structures are shown in Figure S16.

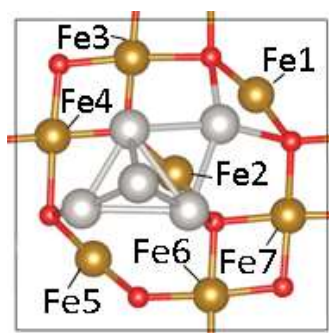


Figure S15. The non-equivalent Fe atoms in the first and second atomic layers of the Pt₅/Fe₃O₄ structure shown in Figure 4(a).

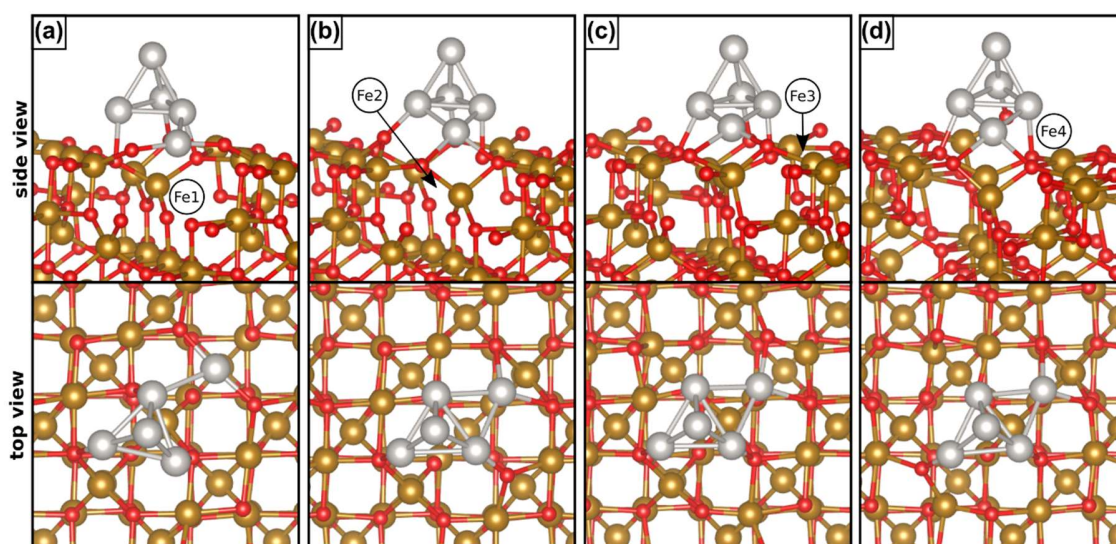


Figure S16. The optimized structures of Fe vacancies in the first layer of the Pt₅/Fe₃O₄ structure shown in Figure 4 (a).

The formation energy of the iron vacancy (E_f), given in Table S11, has been calculated according to the following equation:

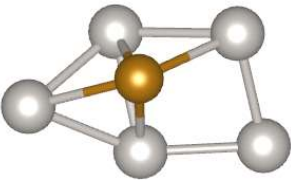
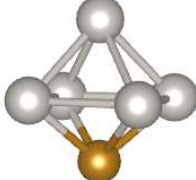
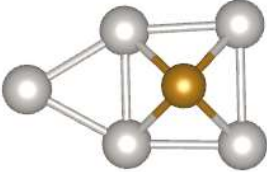
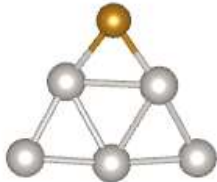
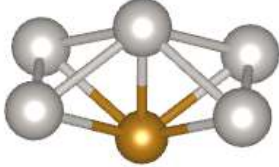
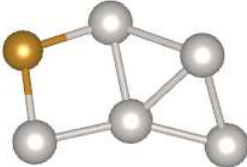
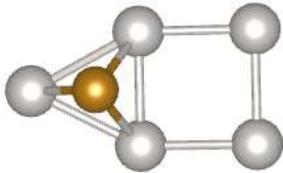
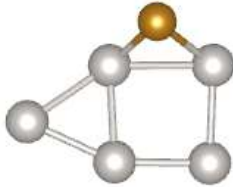
$$E'_f = E[(\text{Pt}_5/\text{Fe}_{3-x}\text{O})] + E[\text{Fe}(\text{g})] - E[(\text{Pt}_5/\text{Fe}_3\text{O}_4)] \quad (7)$$

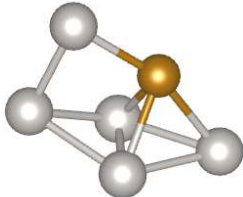
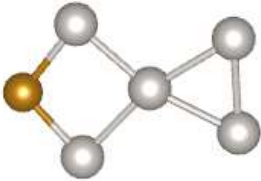
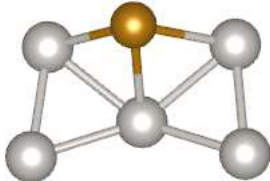
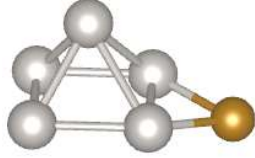
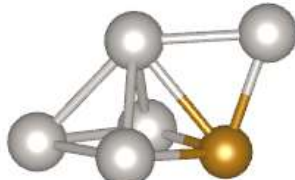

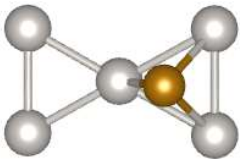
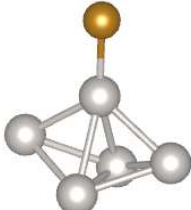
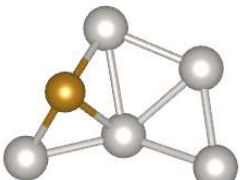

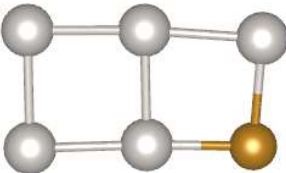
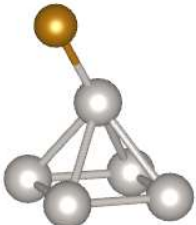
Table S11. Fe vacancy energy (E_f , eV) and total spin magnetic moment per unit cell (M , μ_B).

| | Figure | E_f | M_{total} |
|------------------|---------|-------|--------------------|
| V_{Fe1} | S15(a) | 6.70 | 4.84 |
| V_{Fe2} | S15 (b) | 6.90 | 3.64 |
| V_{Fe3} | S15 (c) | 7.69 | 2.52 |
| V_{Fe4} | S15 (d) | 6.37 | 2.87 |

We then consider the preferred adsorption sites for a single Fe atom on the various isomers of Pt_5 in the gas phase. Altogether, we have considered 20 possible isomers. Table S12 reports the optimized structures and their relative energy (E_R). The binding energy of Fe to Pt_5 in the most stable isomer is -0.99 eV.

Table S12. Relative energy (E_R) of an adsorbed Fe atom on Pt_5 clusters.

| Structure | E_R , eV | Structure | E_R , eV |
|---|------------|---|------------|
|  | 0.00 | 11  | 0.82 |
|  | 0.06 | 12  | 0.95 |
|  | 0.16 | 13  | 1.04 |
|  | 0.23 | 14  | 1.10 |

| | | | | | |
|----|---|------|----|--|------|
| 5 |  | 0.28 | 15 |  | 1.49 |
| 6 |  | 0.39 | 16 |  | 1.76 |
| 7 |  | 0.49 | 17 |  | 2.39 |
| 8 |  | 0.56 | 18 |  | 2.71 |
| 9 |  | 0.69 | 19 |  | 2.74 |
| 10 |  | 0.73 | 20 |  | 2.76 |

We now consider the energetic cost of displacing the Fe1 (tetrahedral) and Fe4 (octahedral) atoms, indicated in Figure S15, from the support and adsorbing it on the Pt₅ cluster. The Fe atom has been re-adsorbed on various sites of the supported Pt₅ cluster, starting from the most stable structure (Figure 4 (a) in the main text). Figure S17 (a)-(c) and (e)-(f) shows the optimized structures. Based on our results for the Pt₅Fe gas phase isomers (Table S12), the re-adsorption of the Fe atom on the triangular facet of a supported Pt₅(i) cluster, Figure 4 (c), has also been studied. Figure S17 (d) shows the optimized structure.

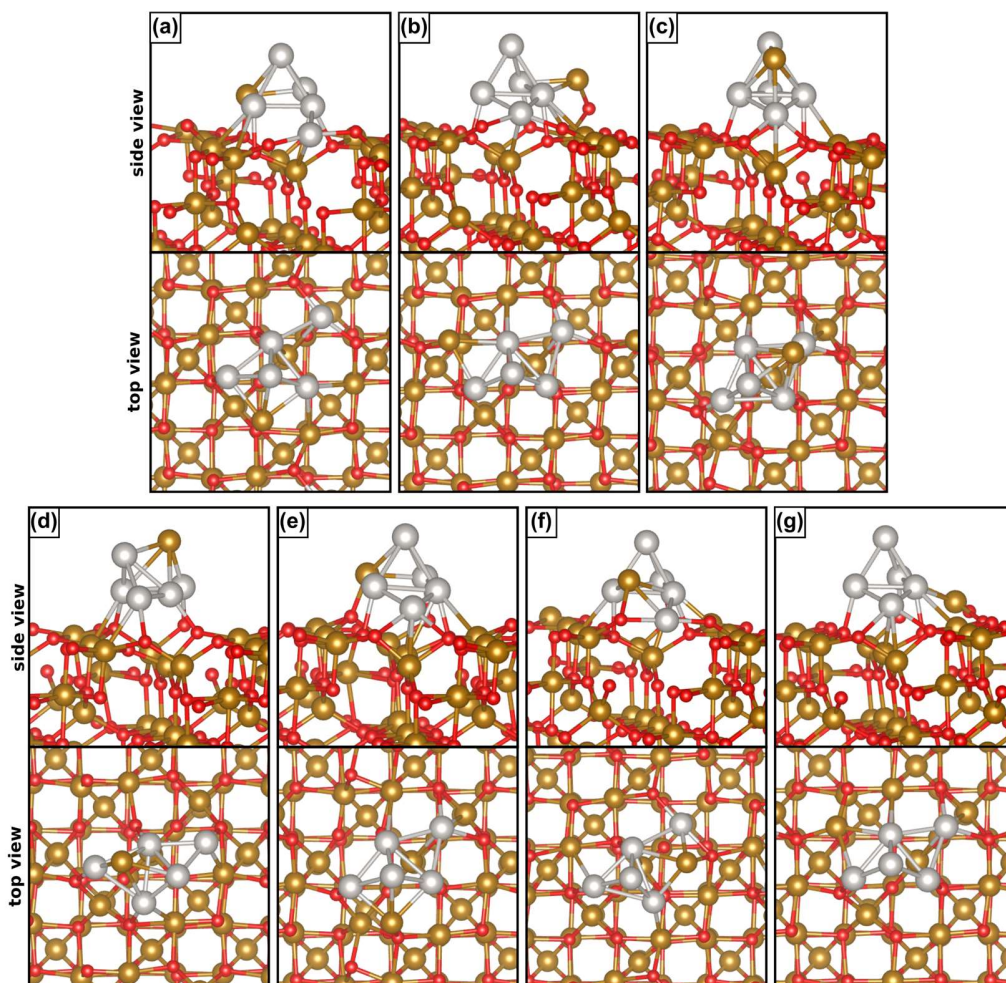
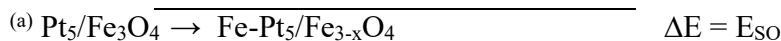


Figure S17. Various isomers of Pt₅Fe supported on Fe₃O₄.

Table S13. Fe spillover energy (E_{SO} , eV) and its site shown in Figure S15 and total spin magnetic moment per unit cell (M , μ_{B}).

| Figure | Fe site | $E_{\text{SO}}^{(a)}$ | M_{total} |
|------------------------|---------|-----------------------|--------------------|
| S16 (a) | Fe1 | 2.38 | 4.83 |
| S16 (b) | Fe1 | 2.53 | 4.07 |
| S16 (c) | Fe4 | 2.61 | 3.23 |
| S16 (d) | Fe4 | 3.18 | 1.75 |
| S16 (e) | Fe4 | 3.38 | 4.17 |
| S16 (f) | Fe1 | 4.17 | 3.57 |
| S16 (g) ^(b) | Fe4 | 0.14 | 3.24 |



^(b) In this case, during the optimization, the Fe atom adsorbed on a triangular facet of Pt_5 moved back to the Fe_3O_4 surface.

In all cases, the Fe spillover implies a remarkable cost (between 2.38 eV and 4.17 eV, depending on the initial and final sites). Case (g) looks like an outlier displaying an almost thermoneutral formation energy, but is in fact a failed attempt, where the Fe ion spontaneously left the Pt_5 cluster and moved back to its lattice site during the relaxation.

Next, we consider the energetic cost of displacing the Fe1 (tetrahedral) or Fe4 (octahedral) atoms (see Figure S15) from the support and adsorbing them on the Pt_5O_3 cluster. The Fe atom has been re-adsorbed on the triangular facet of the supported Pt_5O_3 cluster starting from the most stable structure shown in Figure S13 (a). The results are summarized in Figure S18 and Table S14, indicating a non-favorable process.

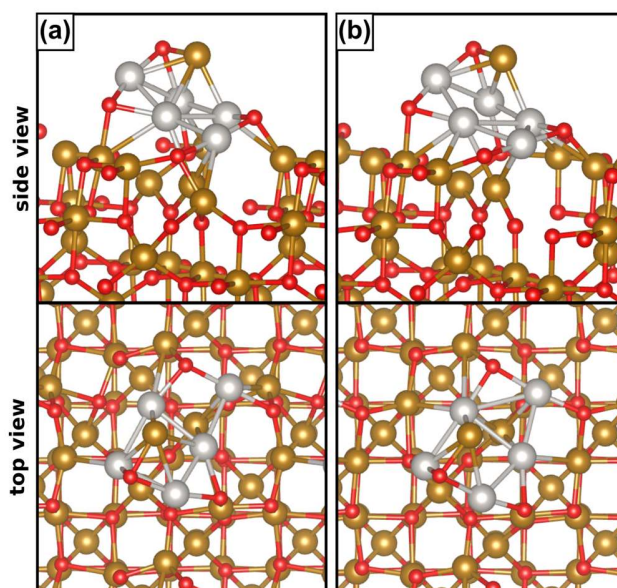


Figure S18. Various isomers of $\text{Pt}_5\text{O}_3\text{Fe}$ supported on Fe_3O_4 .

Table S14. Fe spillover energy (E_{SO} , eV) and its site shown in Figure S15 and total spin magnetic moment per unit cell (M , μ_{B}).

| Figure | Fe site | $E_{\text{SO}}^{(a)}$ | M_{total} |
|---------|---------|-----------------------|--------------------|
| S17 (a) | Fe4 | 2.18 | 2.59 |
| S17 (b) | Fe1 | 3.70 | 4.12 |

^(a) E_{SO} refers to the process: $\text{Pt}_5/\text{Fe}_3\text{O}_4 \rightarrow \text{Pt}_5\text{O}_3\text{Fe}/\text{Fe}_{3-x}\text{O}_{4-y}$

References

- (1) Parkinson, G. S. Iron Oxide Surfaces. *Surf. Sci. Rep.* **2016**, *71* (1), 272–365.
- (2) O'Neill, H. S. C.; Dollase, W. A. Crystal Structures and Cation Distributions in Simple Spinels from Powder XRD Structural Refinements: MgCr_2O_4 , ZnCr_2O_4 , Fe_3O_4 and the Temperature Dependence of the Cation Distribution in ZnAl_2O_4 . *Phys. Chem. Miner.* **1994**, *20* (8), 541–555.
- (3) Bliem, R.; McDermott, E.; Ferstl, P.; Setvin, M.; Gamba, O.; Pavelec, J.; Schneider, M. A.; Schmid, M.; Diebold, U.; Blaha, P.; Hammer, L.; Parkinson, G. S. Subsurface Cation Vacancy Stabilization of the Magnetite (001) Surface. *Science* **2014**, *346* (6214), 1215–1218.
- (4) Hulva, J.; Jakub, Z.; Novotny, Z.; Johansson, N.; Knudsen, J.; Schnadt, J.; Schmid, M.; Diebold, U.; Parkinson, G. S. Adsorption of CO on the $\text{Fe}_3\text{O}_4(001)$ Surface. *J. Phys. Chem. B* **2018**, *122* (2), 721–729.
- (5) Zhang, K.; Shaikhutdinov, S.; Freund, H.-J. Does the Surface Structure of Oxide Affect the Strong Metal-Support Interaction with Platinum? Platinum on $\text{Fe}_3\text{O}_4(001)$ versus $\text{Fe}_3\text{O}_4(111)$. *ChemCatChem* **2015**, *7* (22), 3725–3730.
- (6) Kelemen, S. R.; Kaldor, A.; Dwyer, D. J. The Adsorption of CO on Clean and Potassium Promoted FeO Surfaces. *Surf. Sci.* **1982**, *121* (1), 45–60.
- (7) Sebetci, A. A Density Functional Study of Bare and Hydrogenated Platinum Clusters. *Chem. Phys.* **2006**, *331* (1), 9–18.
- (8) Xiao, L.; Wang, L. Structures of Platinum Clusters: Planar or Spherical. *J. Phys. Chem. A* **2004**, *108* (41), 8605–8614.
- (9) Yang, S. H.; Drabold, D. A.; Adams, J. B.; Ordejón, P.; Glassford, K. Density Functional Studies of Small Platinum Clusters. *J. Phys. Condens. Matter* **1997**, *9* (5), L39–L45.
- (10) Heredia, C. L.; Ferraresi-Curotto, V.; López, M. B. Characterization of Pt_N ($N=2-12$) Clusters through Global Reactivity Descriptors and Vibrational Spectroscopy, a Theoretical Study. *Comput. Mater. Sci.* **2012**, *53* (1), 18–24.
- (11) Bhattacharyya, K.; Majumder, C. Growth Pattern and Bonding Trends in Pt_n ($n = 2-13$) Clusters: Theoretical Investigation Based on First Principle Calculations. *Chem. Phys. Lett.* **2007**, *446* (4–6), 374–379.
- (12) Grönbeck, H.; Andreoni, W. Gold and Platinum Microclusters and Their Anions: Comparison of Structural and Electronic Properties. *Chem. Phys.* **2000**, *262* (1), 1–14.
- (13) Sebetci, A.; Güvenç, Z. B. Energetics and Structures of Small Clusters: Pt_N , $N = 2-21$. *Surf. Sci.* **2003**, *525* (1–3), 66–84.